Frederico Botelho da Costa

Licenciado em Ciências da Engenharia Física

Development and Study of a Non-Destructive Testing System with Terahertz Radiation

Dissertation submitted in partial fulfillment
of the requirements for the degree of

Master of Science in
Engineering Physics

Advisers: Telmo Santos, Professor Associado com Agregação, NOVA University of Lisbon
Pedro Vieira, Professor Auxiliar, NOVA University of Lisbon

Examination Committee

Chair: André Wemans
Rapporteurs: Grégoire Bonfait
Members: Telmo Santos

FACULDADE DE CIÊNCIAS E TECNOLOGIA
UNIVERSIDADE NOVA DE LISBOA

January, 2021

Development of a Non-Destructive Testing System with Terahertz Radiation

This document was created using the (pdf)LaTeX processor, based on the "novathesis" template[1], developed at the Dep. Informática of FCT-NOVA [2].
[1] https://github.com/joaomlourenco/novathesis [2] http://www.di.fct.unl.pt

Acknowledgements

First, I would like to thank the institution, Faculdade de Ciências e Tecnologia da Universidade Nova de Lisboa, for providing me such a complete education in an environment that promotes the well being and socialisation between students.

I would like to show my great appreciation for my advisers professor Telmo Santos and professor Pedro Vieira, for guiding me and keeping me motivated in my work and research. I would like to thank professor Telmo in particular, for providing me such an interesting working topic, for welcoming me in his laboratory and giving me the freedom, resources and guidance for this exciting work.

I am also grateful to professor Miguel Machado for helping me with the simulations and scans, and for his genuine interest in my work.

My sincere thanks to the professors André Wemans, Gregoire Bonfait and Paulo Ribeiro for dedicating their time to help me with specific problems that emerged in my work.

I must also thank professor Isabel Catarino, for guiding me throughout the course and for always taking time to humour me through my rants and complaints.

I would like to show my gratitude for the PhD students at Núcleo de Tecnologia Mecânica, Edgar Camacho, Francisco Ferreira, Patrick Inácio, Tiago Rodrigues and Valdemar Duarte, for taking me in to the lab, teaching me how to use new tools, and for the occasional "chouriço assado".

I could not go without thanking my good friends Filipe Grilo, Margarida Ribeiro and Daniel Pinheiro, for the support during my thesis work and for putting up with my never-ending barrages of messages.

I would also like to thanks all my other good friends in Engenharia Física, to whom I could dedicate an entire page each. These people provided me with the most enjoyable five years of my life, and without them, I could not have completed this degree.

Finally, I would like to thank both of my parents, for providing me the possibility to get such great education, and for always supporting me in my path.

The author gratefully acknowledges the funding of Project POCI-01-0145-FEDER-016414 (FIBR3D), cofinanced by Programa Operacional Competitividade e Internacionalização and Programa Operacional Regional de Lisboa, through Fundo Europeu de Desenvolvimento Regional (FEDER) and by National Funds through Fundação para a Ciência e a Tecnologia (FCT-MCTES) and Fundação para a Ciência e a Tecnologia (FCT-MCTES) for its financial support via the project UIDB/00667/2020 (UNIDEMI)

Abstract

Continuous wave terahertz imaging is a variant of terahertz imaging that has been made possible with recent advances in technology and has provided interesting results as an inspection method. This variant is more accessible than its counterparts, as such, there is high interest in studying it. This dissertation aims at providing the foundations for the development and use of this technology for Non-Destructive Testing.

The system was assembled and tested for different applications. The fundamental phenomena were studied through experimentation and numerical simulations. A mathematical model was developed to predict the effects of Fabry-Perot interference, a phenomenon that would otherwise be considered undesirable. The comprehension of this effect allows for this method to be used as measuring tool. The system was compared with other non-contact inspection techniques, where it was found to excel at imaging water infiltrations and some composite materials.

Keywords: Terahertz, Continuous-Wave, Imaging, Non-Destructive Testing, Fabry-Perot.

Resumo

Imagiologia por terahertz de onda contínua é uma variante da imagiologia de terahertz que se tornou possível com avanços tecnologicos recentes, que tem mostrado resultados interessantes como técnica de inspeção. Esta técnica é mais acessível que outras variantes e como tal, existe um elevado interesse no seu estudo. Esta dissertação procura estabelecer os fundamentos para o desenvolvimento e aplicação desta técnica para Ensaios Não-Destructivos.

O sistema foi construído e testado em diferentes aplicações. Os fenómenos fundamentais foram estudados através de experimentação e simulações numéricas. Um modelo matemático foi desenvolvido que permite prever o efeito da interferência de Fabry-Perot, fenómeno que é habitualmente considerado indesejado. A compreensão deste efeito permite que este método seja utilizado como ferramenta de metrologia. O sistema foi comparado com outras técnicas de inspeção sem contacto, tendo-se comprovado que se destaca na inspeção de infiltrações de água e alguns materiais compósitos.

Palavras-chave: Terahertz, Onda-Contínua, Imagiologia, Ensaios Não-Destructivos, Fabry-Perot.

Contents

List of Figures

List of Tables

Glossary

C-scan A scan performed along an area. It forms a matrix with a measurement being performed at each point. Produces a 2D images.(1D if taken only in a line)

Acronyms

CNC	Computer Numerical Control
CW	continuous cave
FFF	Fused Filament Fabrication
IMPATT	Impact Ionization Avalanche Trasit-Time
NDT	Non-Destructive Testing
NETD	Noise Equivalent Temperature Difference
NiTi	Nickel Titanium Alloy
PLA	Polylactic Acid
PSF	Point Spread Function
SNR	Signal to Noise Ratio
THz	terahertz

Symbols

A	distance between the source and the sample (see figure 4.1)
α	Lambert-Beer attenuation coefficient
at_i	virtual attenuation coefficient
$\mathbf{B}$	magnetic field
c	speed of light in vacuum
C	distance between the sample and the detector (see figure 4.1)
D	distance between the source and the detector (see figure 4.1)
e	Euler's number
$\mathbf{E}$	electric field
ϵ	relative electric permittivity
ϵ_0	vacuum's electric permittivity
f	transmitance
h	height
I	intensity
j	imaginary identity
k	wave number
κ	extinction coefficient
λ	waveleght

$\mathbf{M}$	magnetization
μ	relative magnetic permeability
μ_0	vacuum's magnetic permeability
n	refractive index
ν	Fresnel parameter
ω	angular speed
$\mathbf{P}$	polarization
ϕ_i	phase lenght
r	reflection coefficient
R	reflectance
σ	electric conductivity
τ	transmited intensity
T	transmitance
θ	angle
V	signal response
x	distance
y	distance
z	distance

Chapter 1

Introduction

Non-Destructive Testing (NDT) is a group of analysis techniques widely used in science and industry. These have the goal of studying the properties, morphology or defects of an object without damaging it or altering it in a way that would affect its function. Such techniques are particularly useful when it is necessary to individually inspect every product at the end of a production line, or to perform periodic analysis of components during their work cycle.

Electromagnetic radiation is a fundamental phenomenon for a number of different testing and imaging techniques, from X-Ray tomography to radar imaging and even visual inspection. Radiation with different frequencies interacts with matter in different ways. Consequently, this sort of interaction can be used to inspect a wide variety of materials.

In this context, terahertz (THz) imaging is a technique of high interest due to its ability to image dielectric parts in depth, similarly to X-ray imaging, whilst not posing the health risks associated with it. Additionally, due to its longer wavelengths, THz shows wave interactions with features at a visible scale. As such, THz waves can show diffraction, refraction and interference, allowing for an analysis that could be complementary to X-ray imaging as is can be seen further on in this work.

The majority of research performed in the field of THz imaging over the last couple of decades, has focused mostly on the *time domain* variant. While this variant provides highly detailed data, it also requires complex and expensive equipment with a large footprint. In contrast, the variant studied in this work, named continuous cave (CW), provides a more accessible and practical solution for an industrial application. The technology used to make this technique more compact and cost-effective is relatively recent,

thus the study of its application is still in its early stages. This was a major motivation for the investigation presented in this work.

This dissertation aims at providing a fundamental study of CW THz. As such, the initial objectives were determined as:

- Develop a working prototype to automate the scanning process for the experiments.
- Test and characterise the response of the system to imaging different defects, features and materials.
- Test resolution enhancing methods, such as deconvolution.
- Compare the performance of the system with other non-contact NDT techniques.
- Numerically simulate the interactions between the radiation and the various materials and features tested.

However, after the Fabry-Perot effect was identified, the following objectives were added:

- Develop and validate a mathematical model that accurately describes the Fabry-Perot effect.
- Evaluate the effect of this phenomenon on the imaging of features and defects.
- Test the possibility of using this effect for a metrology application.

To support such studies, a prototype was built and tested. The results were used to create a mathematical model that can predict some of the involved phenomena, namely the Fabry-Perot effect.

To situate the technology in the area of non-destructive testing, the prototype was compared with other non-contact imaging systems, using a sample designed and created for the purpose.

A better understanding and prediction of the system can be obtained through numerical simulations. As such, various effects observed experimentally were analysed by *Finite Element Analysis*.

1.1 Deriving Articles

The work presented in this thesis brought some advancements to the state of the art of the technology. As such, a manuscript was written which is currently under review in the journal "Measurement".

Frederico B. Costa, Miguel A. Machado, Pedro Vieira, Telmo G. Santos. *Continuous Wave Terahertz Imaging for NDT: Fundamentals and Experimental Validation*. Journal of the International Measurement Confederation. Submitted in 27/10/2020.
For the full manuscript, go to:

`https://drive.google.com/drive/folders/1ZOPmxCUo6-YF5yFV_M5JnOHRooUUWMqd?usp=sharing`

The journal:

`https://www.journals.elsevier.com/measurement`

Impact Factor: 3.364

Chapter 2

State of the Art

Traditionally, the controlled production of radiation was divided into two domains, the electronic, that covered long waves from radio to microwaves, and the photonic domain, stretching from infra-red into gamma rays [1]. However, amidst the aforementioned bands there is a range, known today as terahertz, which wavelengths are in the order of millimetres (0.1 to 10 THz). The name terahertz refers to the frequency of 10^{12} hertz. The controlled production of these waves proved to be difficult for the technology from either domain, since the frequency was too high for electronic systems and too low for optoelectronics and lasers [2], hence it was known as the "terahertz gap". It was only in the beginning of the seventies, with the works of Auston D. H. *et al.* [3] and Yang K. H. *et al.* [4], that the production of such waves became convenient as the first laser based terahertz sources were made.

The interaction between terahertz and matter is similar to the one with longer waves, in the sense that the radiation permeates easily trough dielectric materials while being highly reflected by conductive materials and highly absorbed by water [5]. Despite the low attenuation in dielectric mediums, these present a refractive index significantly distinct from the one on air. Consequently, the interaction is similar to the one between visible light and glass, in the sense that the radiation refracts on interfaces with little amplitude loss in the medium. As such, it is ideal for imaging these materials. It is also important to note that the shorter wavelength makes it so images can be produced with much finer resolution than if longer waves were to be used [6].

One could argue that because X-rays have a much smaller wavelength and permeate through a wider variety of materials, X-ray imaging would be a superior technique for any situation. However, while a traditional X-ray image is obtained only by the difference

in absorption of its rays through a medium, on terahertz, because the wavelength is of similar dimensions as the observed defects and features, diffraction becomes a bigger factor on the passing radiation. This phenomenon allows small defects to have a large impact on the image, making them more easily identified. Additionally, terahertz waves are absorbed differently by some materials, which can produce contrasts that would be impossible with X-rays, as it can be seen further on with the case of water. As such, these techniques could potentially be complementary. It is also important to note that terahertz radiation is non-ionizing and thus does not pose a threat to the health of the operands [7].

Throughout the last few decades, a variety of different terahertz imaging systems have been developed. Mittleman [1] describes the essential components of a *time domain imaging system* as seen in the figure 2.1a.

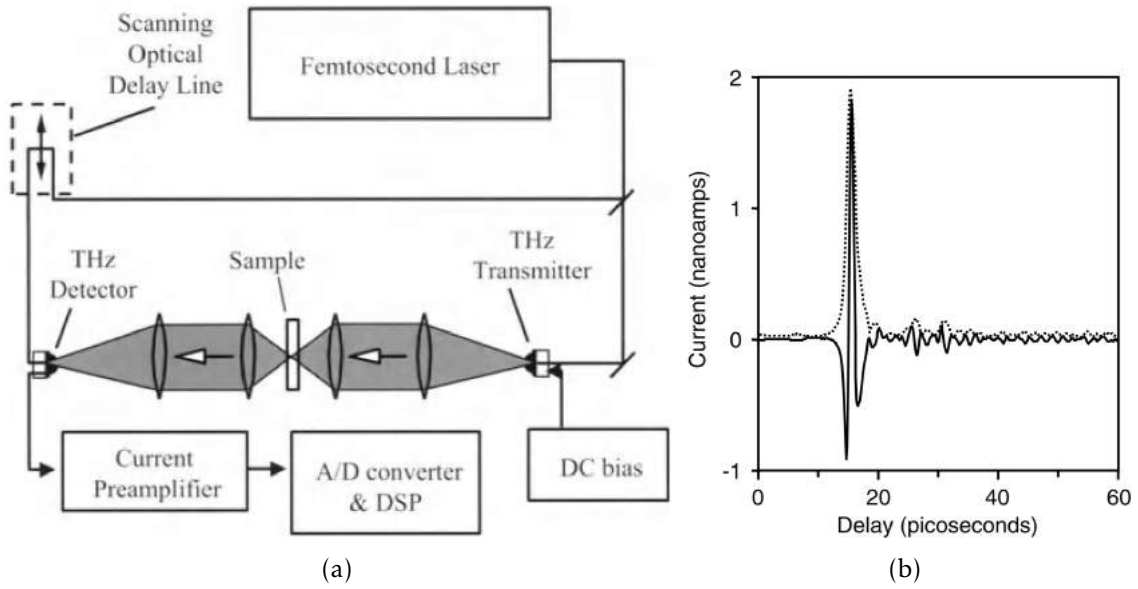

(a) (b)

Figure 2.1: Time-Domain systems and acquired data. (a) Schematic of a time domain imaging system. (b) Waveform obtained with a time domain system. Adapted from [1].

Approaches such as the one shown above, require a pulsed radiation source operating in femtosecond pulses. Using an optical delay line it is possible to acquire the waveform after it traverses the sample and hits the detector (figure 2.1b). From this acquisition, an assortment of data can be extracted such as amplitude, phase and delay of the pulse. By acquiring this information in an array of spacial points (C-scan), different images can be produced starting from a single set of data. Figure 2.2, shows two images of a chocolate bar that contains almonds inside the chocolate and a logotype embossed onto the surface. One of the images is produced by the amplitude loss, while the other is generated by the travel time of the wave. On the one built by amplitude, the almonds are more visible as these posses a higher water content which highly absorbs terahertz. On the image produced by travel time, the logotype is more perceivable, as light takes a longer time permeating through thicker material.

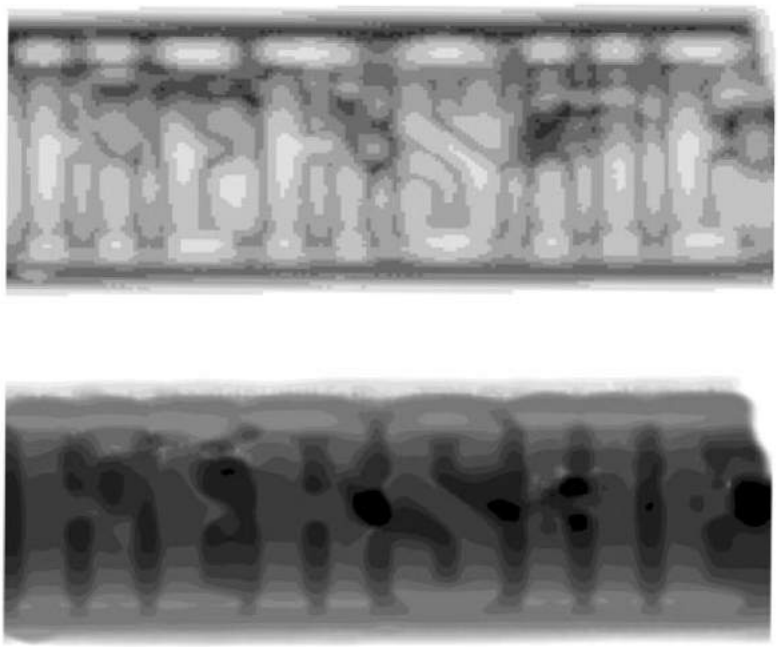

Figure 2.2: Two THz images of a same chocolate bar. The bar contains almonds and has a logotype embossed on the surface. The image on top was built from the amplitude of the acquired waves while the bottom one was made from the delay times of the wavefronts [1].

In other approaches, the acquired radiation is reflected by the sample instead of transmitted through. This technique is particularly useful when the material is laminated (figure 2.3), since the radiation is reflected on each interface and thus producing a reflected wave for each layer. Additionally, this setup enables analysis in situations where only one of the sample's surfaces is accessible [8]–[10].

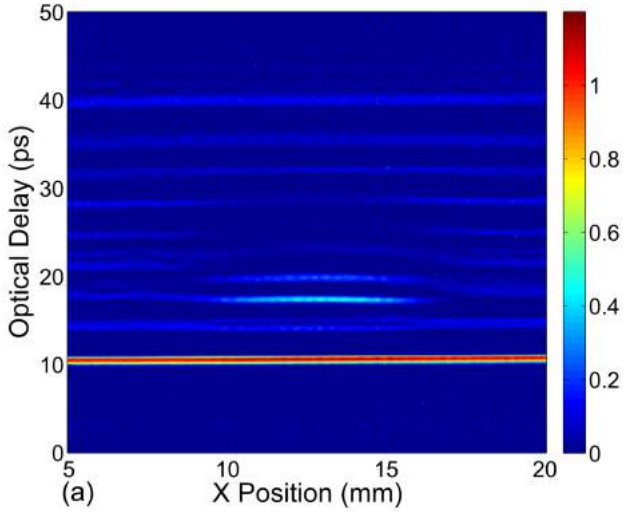

Figure 2.3: Image of a line of a laminated composite material acquired by reflection. The visible lines correspond to different times of arrival of the pulse by being reflected by the different interfaces. Retrieved from [10].

Despite having the clear advantage of collecting a variety of data, the time domain approach requires a highly complex, delicate and costly system. Nevertheless, most research on terahertz imaging focuses on this variant.

In *continuous wave terahertz imaging*, a longer pulse of radiation is emitted, while simultaneously, a detector measures the intensity of radiation that permeates through the sample. Variations of intensity indicate different effects of attenuation and dispersion of the incident radiation, and thus the morphology and constitution of the material can be inferred on. While acquiring less detailed data, *continuous wave* (CW) systems prove to present a simpler, more affordable, quick and compact solution when compared to their *time domain* counterparts [11], [12].

This approach was employed on the 2002 article by Karsten J. Siebert *et al.* [13] where a Ti:Sapphire laser was used as a terahertz source to obtain a continuous wave transmission image of a canary's skull, which was comparable to one produced with X-ray imaging (figure 2.4).

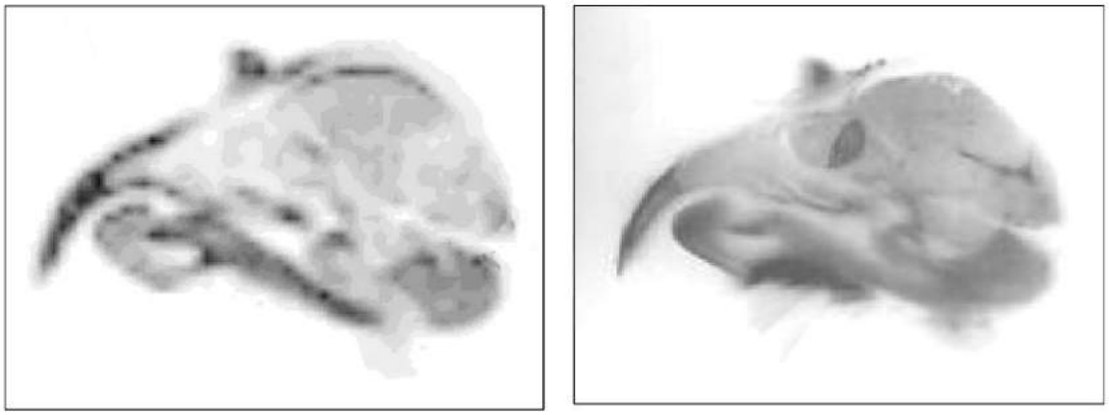

(a) (b)

Figure 2.4: Imaging of a canary's skull. (a) Continuous wave terahertz image of a canary's skull. (b) X-ray image of the same skull. Adapted from [13].

In recent years, the advances in Gunn diodes and the development of technologies such as *Impact Ionization Transit Time* (IMPATT) diodes (used in this work), have popularised the use of this approach as it is seen numerous articles [11], [14]–[17].

On the 2009 article, Y. Oyama *et al.* [17] study CW THz images of water infiltrations. Figure 2.5 shows an image where water was injected into a wood sample and set to dry. A 0.2 THz source was used to image the piece, allowing for the water distribution during the drying process to be observed. On the same article, water droplets were poured on a cracked concrete sample, allowing the water to infiltrate into the fissure. Figure 2.6 shows this process and the results. This method allowed for the inspection of a defect that would otherwise not be visible.

More recently, in 2017, Hai Zhang *et al.* [15] conducted a study of a canvas painting

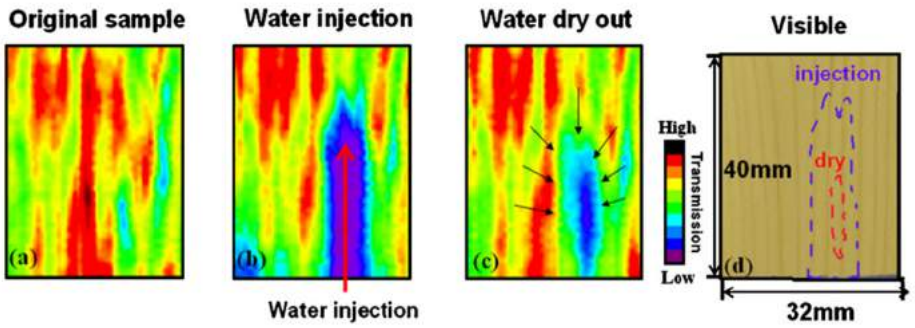

Figure 2.5: Terahertz image of a water infiltration in wood as it dries out. Adapted from [17].

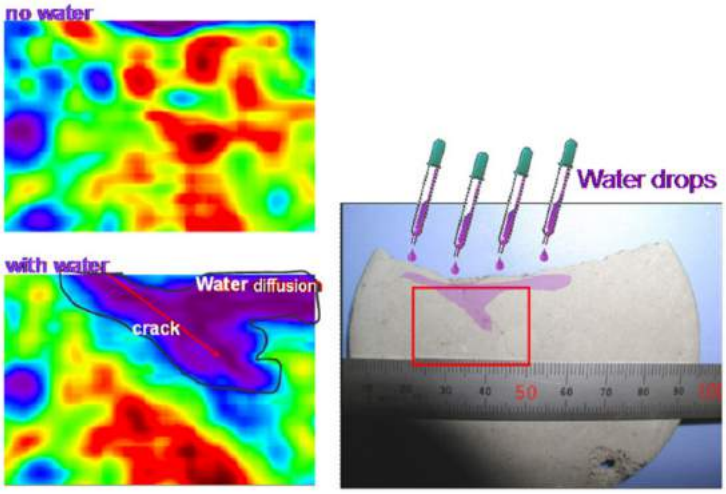

Figure 2.6: Terahertz image of water infiltrating in a concrete crack. Adapted from [17].

using continuous wave terahertz imaging. In their setup, a diode based source and detector were used. The source diode was an IMPATT diode, technology which is proprietary to the company *TeraSense*, from where the source and detector used in the work described by this thesis were also acquired.

CW THz can also be applied in a reflection setup. On the 2019 conference paper by T. Tanabe [18], a 0.14 THz IMPATT source is used to image a variety of materials in reflection. Figure 2.7 shows a reflection image of a copper cable where one of the conductors is increasingly ruptured through traction. The imaging allows for inspection underneath the opaque polymeric insulation at the various stages of traction.

On the same work, a study was conducted on the reflectivity of steel rods depending on their corrosion. Through these scans, as figure 2.8 shows, it is possible to identify and locate the corroded steel rods inside concrete as these are less reflective than non-corroded ones.

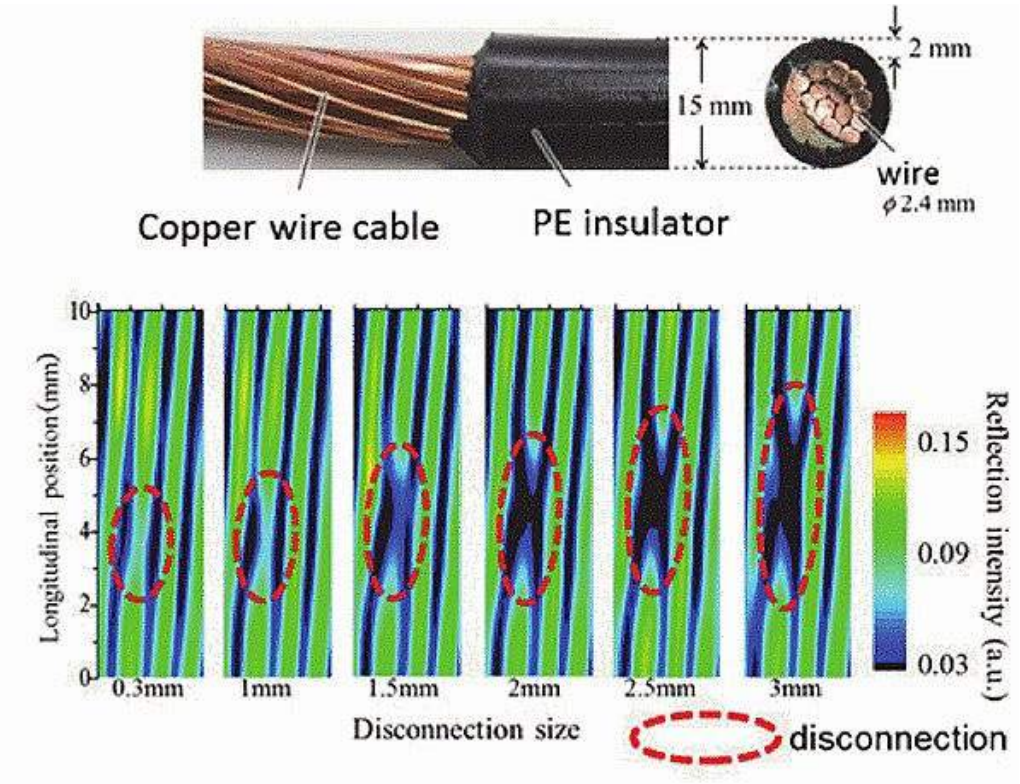

Figure 2.7: CW reflection THz image of an electrical cable where one of the conductors is being ruptured. Adapted from [18].

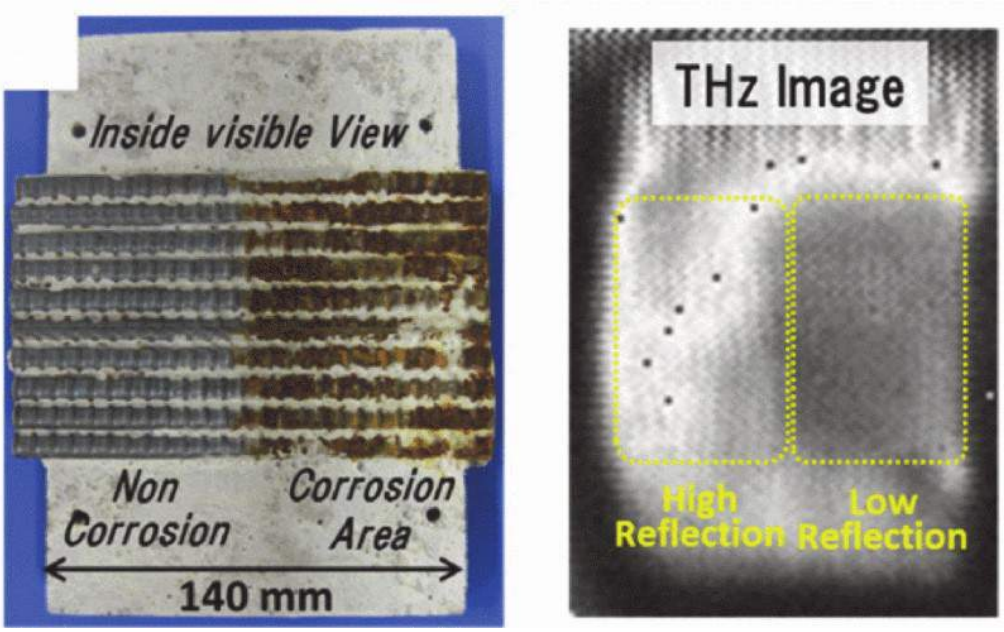

Figure 2.8: CW reflection THz image steel rods in concrete. Some of the rods are corroded which makes them less reflective resulting in a darker image. Adapted from [18].

Chapter 3

Electromagnetic Radiation Imaging Systems

3.1 Introduction

Throughout the last century, as technology evolved, the production and detection of radiation gradually reached almost the entire electromagnetic spectrum. Consequently, a variety of imaging techniques were developed. Generally, the image is built from measuring the radiation that is transmitted, reflected, refracted or emitted by the imaged object.

A basic approach to imaging consists in distributing the collected data through a matrix according to its relative position (C-scan). However, in situations where the detector is not punctual and the area of collection of each point overlaps with the neighbouring points, the final image will appear blurred and poorly defined even with a high pixel density. To combat this issue, deconvolution filters can be applied to the image.

Another factor that can impact the resolution of the image is the wavelength of the involved radiation. When electromagnetic waves interact with a feature or defect with dimensions equal or inferior to that to the wavelength, the waves will diffract, and the object will project a diffraction pattern instead of a shadow. It is possible to counteract the effects of diffraction through the use of a *point spread function* that takes the wavelength into consideration, by deconvolving the image. However, this solution is only applicable in situations where the light source is monochromatic and coherently polarised [19], and thus will not be studied in this work.

3.2 Electromagnetic Waves

To discuss terahertz waves, as we would with any other electromagnetic wave, one should start with the basic Maxwell equations [20], that in vacuum differential form are written as

$$\nabla \cdot \mathbf{E} = 0, \tag{3.1}$$

$$\nabla \cdot \mathbf{B} = 0, \tag{3.2}$$

$$\nabla \times \mathbf{E} = -\frac{\partial \mathbf{B}}{\partial t}, \tag{3.3}$$

$$\nabla \times \mathbf{B} = \mu_0 \epsilon_0 \frac{\partial \mathbf{E}}{\partial t}, \tag{3.4}$$

where **E** represents the electric field, **B** the magnetic field, ϵ_0 and μ_0 vacuum's permittivity and permeability respectively. These variables, as well as the remaining in this chapter, are presented in S.I. units. Despite their size, along with the equation for Lorentz force

$$\mathbf{F} = q(\mathbf{E} + \mathbf{v} \times \mathbf{B}), \tag{3.5}$$

where **v** represents the velocity of the charge, these expressions translate the entirety of basic electrodynamics. The electric **E** and magnetic **B** fields can also be represented in their general form

$$\mathbf{D} \equiv \epsilon_0 \mathbf{E} + \mathbf{P} = \epsilon \mathbf{E}, \tag{3.6}$$

$$\mathbf{H} \equiv \frac{1}{\mu_0}\mathbf{B} - \mathbf{M} = \frac{1}{\mu}\mathbf{B}, \tag{3.7}$$

where **P** and **M** represent the polarisation and magnetisation of the medium respectively, and ϵ and μ represent the electric permittivity and magnetic permeability of the medium respectively.

3.2.1 The Wave Equation

Using the vectorial identity

$$\nabla \times (\nabla \times \mathbf{X}) = \nabla(\nabla \cdot \mathbf{X}) - \nabla^2 \mathbf{X}, \tag{3.8}$$

on the electric field **E**, and using the relation in (3.3) we obtain

$$\begin{aligned} \nabla \times (\nabla \times \mathbf{E}) = \nabla(\nabla \cdot \mathbf{E}) - \nabla^2 \mathbf{E} &= \nabla \times \left(-\frac{\partial \mathbf{B}}{\partial t} \right) \\ &= -\frac{\partial}{\partial t}(\nabla \times \mathbf{B}) = \mu_0 \epsilon_0 \frac{\partial \mathbf{E}}{\partial t}. \end{aligned} \tag{3.9}$$

Applying the same vectorial identity to the magnetic field **B**, and the relation (3.4), we obtain:

$$\begin{aligned}\nabla \times (\nabla \times \mathbf{B}) = \nabla(\nabla \cdot \mathbf{B}) - \nabla^2 \mathbf{B} = \nabla \times \left(\mu_0 \epsilon_0 \frac{\partial \mathbf{E}}{\partial t}\right) \\ = \mu_0 \epsilon_0 \frac{\partial}{\partial t}(\nabla \times \mathbf{E}) = \mu_0 \epsilon_0 \frac{\partial \mathbf{B}}{\partial t}.\end{aligned} \tag{3.10}$$

Since $\nabla \cdot \mathbf{E} = 0$ and $\nabla \cdot \mathbf{B} = 0$, the decoupled wave equations for each component can be derived,

$$\nabla^2 \mathbf{E} = \mu_0 \epsilon_0 \frac{\partial^2 \mathbf{B}}{\partial t^2}, \quad \nabla^2 \mathbf{B} = \mu_0 \epsilon_0 \frac{\partial^2 \mathbf{E}}{\partial t^2}. \tag{3.11}$$

In a dielectric material, the permissivity and permiability values ϵ_0 and μ_0, would be replaced by their relative counterparts ϵ and μ. In this situation the speed of propagation of the waves can be related as follows

$$v = \frac{1}{\sqrt{\mu\epsilon}} = \frac{c}{n}, \tag{3.12}$$

where c is the speed of light in vacuum and n the refractive index of the material that establishes the relation between the the speed of light in this material and in vacuum.

For plane waves, the wave equation has the generic solutions

$$\mathbf{E}(\mathbf{r}, t) = \mathbf{E}_0 e^{j(\mathbf{k}\cdot\mathbf{r} - \omega t)} \quad \textit{and} \quad \mathbf{B}(\mathbf{r}, t) = \mathbf{B}_0 e^{j(\mathbf{k}\cdot\mathbf{r} - \omega t)}. \tag{3.13}$$

where k represents the wave number, ω the angular frequency and j the complex identity. Substituting (3.13) for $\nabla \cdot \mathbf{E} = 0$ and $\nabla \cdot \mathbf{B} = 0$ the following relations emerge

$$\mathbf{k} \cdot \mathbf{E} = 0 \quad \textit{and} \quad \mathbf{k} \cdot \mathbf{H} = 0, \tag{3.14}$$

These relations indicate that the waves are transverse, i.e., they oscillate perpendicularly to their direction of propagation. The two components are tightly related by the Maxwell equations in the sense that when one is known, the other can be unmistakably determined. And so the two components induce each other mutually and propagate coupled. The two coupled components are called an *electromagnetic wave*.

3.2.2 Reflection

When a beam of radiation transverses from a material to another where it propagates at a different speed, it will suffer refraction and reflection on the interface as it is shown in figure 3.1.
The angle at which the beam is refracted can be determined by Snell's law

$$n_1 \sin\theta_i = n_2 \sin\theta_r, \tag{3.15}$$

where n_1 e n_2 represent the refractive indexes of the mediums, θ_i the angle of the incident beam relative to the surface's normal and θ_r the angle of the refracted beam.

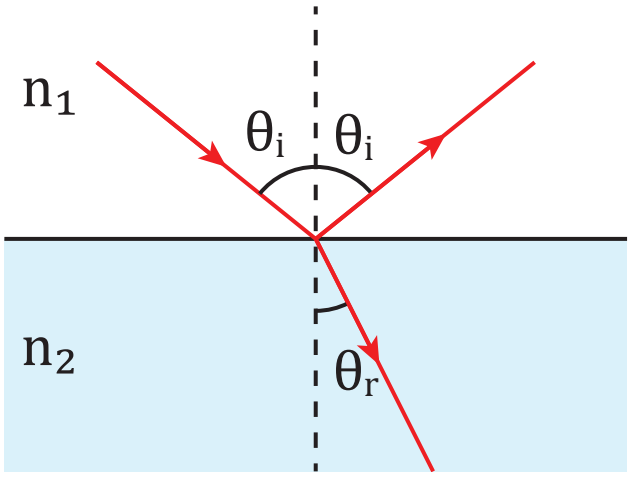

Figure 3.1: Refraction and reflection of a beam of light.

Reflectance R and transmitance T are defined as the relation between incident power E_I and reflected E_R or transmitted E_T respectively [21]. These relations are defined as

$$R = \frac{|E_R|^2}{|E_I|^2} \quad and \quad T = \frac{n_2|E_T|^2}{n_1|E_I|^2}. \tag{3.16}$$

Replacing the equation (3.13) in (**??**), the dispersion relation is obtained

$$k^2 = \epsilon\mu\omega^2. \tag{3.17}$$

This relation dictates how a wave with a certain frequency propagates in a medium. It is important to note the dependency this relation has with the electric and magnetic properties. In a non-magnetic material, k can be related with the wavelength λ as follows

$$k = \frac{2\pi}{\lambda} = n\frac{\omega}{c}, \tag{3.18}$$

thus also relating to the frequency. In a conductive medium, where the electrical conductivity is high so that $\sigma \gg \omega\epsilon$, the dispersion equation (3.17) can be approximated to

$$k^2 \approx j\sigma\mu\omega, \tag{3.19}$$

j being the complex unit. The amplitude of k is then given by

$$k \approx \sqrt{\frac{\omega\mu\sigma}{2}}(1+j). \tag{3.20}$$

The previous expression indicates that the amplitude of the radiation decays exponentially as in travels through the material. This effect is called *skin effect* [22]. The depth at which the amplitude of the wave becomes $\frac{1}{e}$ of the amplitude on the surface is called *skin depth* and is given by

$$\delta = \sqrt{\frac{2}{\omega\mu\sigma}}. \tag{3.21}$$

The expression above indicates that the skin depth is larger for longer wavelengths and so it could be expected that the transmittance would be higher for these low frequencies. However, the opposite occurs which can be justified by the fact that in order to propagate through a material, a wave requires to penetrate a depth equal or greater than its wavelength [21]. Consequently, only waves from the energy range of X-rays and above can propagate through metallic materials.

Being highly impermeable to terahertz does not mean that metallic materials absorb its incident energy. The skin effect causes a refractive index $n \gg 1$ which leads to a high reflectivity. For this reason, in metals, the energy is mostly reflected.

A particular case of reflection that proved relevant for this work is the one that takes place in Fabry-Perot interferometers. The simplest instance of this effect occurs in a scenario where three materials are set so that the two interfaces are parallel, as shown in figure 3.2.

For an incident wave $E_{in} = e^{j(\omega t - kz)}$ propagating perpendicular to the interfaces, we define a transmitance $f = \sqrt{1 - r^2}$ where r is the reflection coefficient given by

$$r = \frac{|n_1 - n_2|}{n_1 + n_2}, \tag{3.22}$$

being that n_1 and n_2 correspond to the refractive indexes of the media. If we define the zero of the z axis in the first interface, the electric field will be $e^{j\omega t}$ right before it and $f_1 e^{j\omega t}$ right after [23]. By the same logic, right after the second interface, the electric field will be given by

$$E_1 = f_1 f_2 e^{j(\omega t - kd)}. \tag{3.23}$$

The reflected wave, will also reflect back at the first interface, producing a second forward moving wave, that will interfere with the original. This second beam is given by

$$E_2 = f_1 f_2 r_1 r_2 e^{j(\omega t - 3kd)} = E_1 r_1 r_2 e^{-2jkd}. \tag{3.24}$$

This re-reflected beam, will also be partially reflected and so, infinite beams $E_3, E_4, ..., E_n$ with ever smaller amplitudes will be produced. The resulting electric field right after the second interface will be given by

$$E_{out} = \sum_{n=1}^{\infty} E_n = E_1 \sum_{n=1}^{\infty} (r_1 r_2)^{(n-1)} e^{-j2kd(n-1)} = E_1 \sum_{n=1}^{\infty} (r_1 r_2 e^{-j2kd})^n = \frac{E_1}{1 - r_1 r_2 e^{-j2kd}}. \tag{3.25}$$

And thus, the intensity of the transmitted beam is

$$\frac{I_{out}}{I_{in}} = \frac{E_{out}E_{out}^*}{E_{in}E_{in}^*} = \frac{(1-r_1r_2)^2}{(1-r_1r_2)^2 + 4r_1r_2\sin^2(kd)}. \tag{3.26}$$

The Fabry-Perot effect thus results in a system with a transmissivity that is highly dependant on the distance between the interfaces. Figure 3.2 (b) shows the relation between the transmissivity and the distance between interfaces. It is important to remember that the wave number k is dependent on the frequency of the radiation and on the characteristics of the medium.

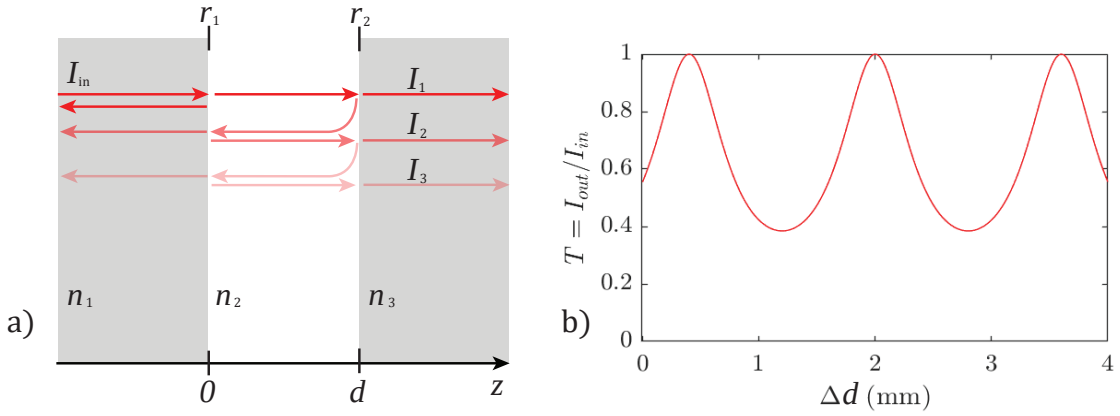

Figure 3.2: Schematic of Fabry-Perot interference, and the resulting plot produced by equation (3.26).

3.2.3 Attenuation

On the previous sections, the refractive index n is considered for an ideal material where the energy absorption is not contemplated. On a more realistic approach [23], the refractive index can be defined as a complex number:

$$n = n_{Real} + j\kappa. \tag{3.27}$$

On the expression above, κ represents the complex component of the refractive index named *extinction coefficient*.

Similar to other physical phenomena, it can be experimentally observed [24] that the amplitude of an electromagnetic wave decays as it propagates though a medium according to Lambert-Beer's law

$$I = I_0 e^{-\alpha x}, \tag{3.28}$$

where I is the intensity at a given depth x, I_0 the intensity of the incident radiation and α the attenuation coefficient. This coefficient can be related to the complex component of the refractive index κ according to the equation

$$\alpha = \frac{4\pi\kappa}{\lambda_0}, \tag{3.29}$$

where λ_0 is the wavelength of the referred radiation in vacuum.

On the plot in figure 3.3 the absorbance spectrum is represented on the terahertz range. Remembering that higher frequencies allow for higher resolution images, it is interesting to note the compromise between resolution and signal attenuation, being that these have inverse behaviours as frequency rises.

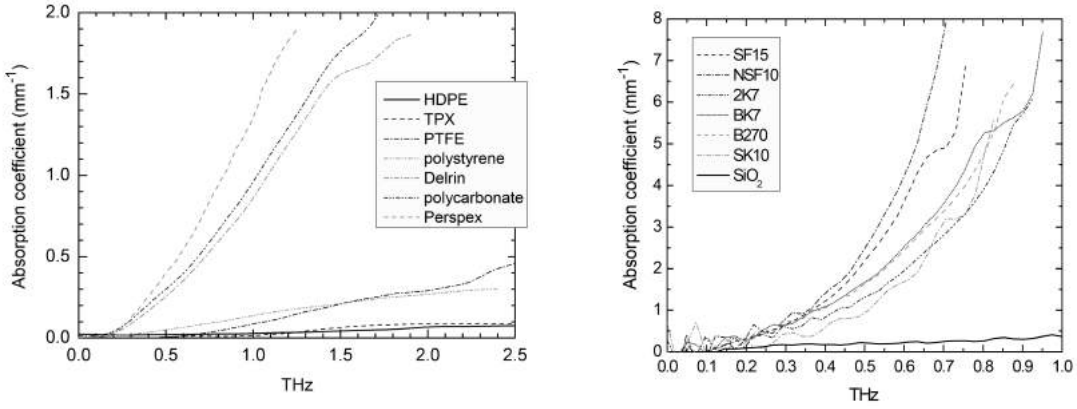

(a) (b)

Figure 3.3: (a) Absorbance spectra for different polymers. (b) Absorbance spectra for different glasses for the terahertz range [25].

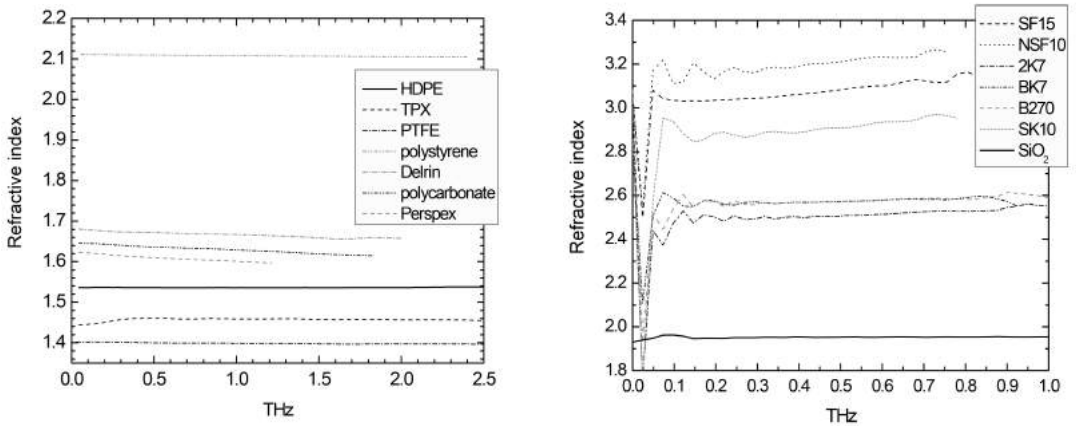

(a) (b)

Figure 3.4: (a) Refractive index spectra for different polymers. (b) Refractive index spectra for different glasses for the terahertz range [25].

It is also relevant to note (figure 3.4) that despite being approximately constant along the frequency, the refractive indexes for these materials are considerably superior to 1. Since at 0.1 THz, frequency used in the experiments of this work, the attenuation is

low and the refractive index is high, refraction is expected to have a higher impact than absorption when it comes to distinguishing morphological features.

3.2.4 Diffraction

From the perspective of light as particles, one could assume that when a collimated beam is shined onto an obstacle, a shadow would be cast forward in the direction of propagation of the beam (figure 3.5a). However, in reality light can be measured to hit the area where a shadow would be expected, a phenomenon which is most prevalent the narrower the object is when compared to the wavelength. This occurrence can be justified by the wave behaviour of light, where the wave-front that passes at the edges of the obstacle behaves as point light source as shown in figure 3.5b.

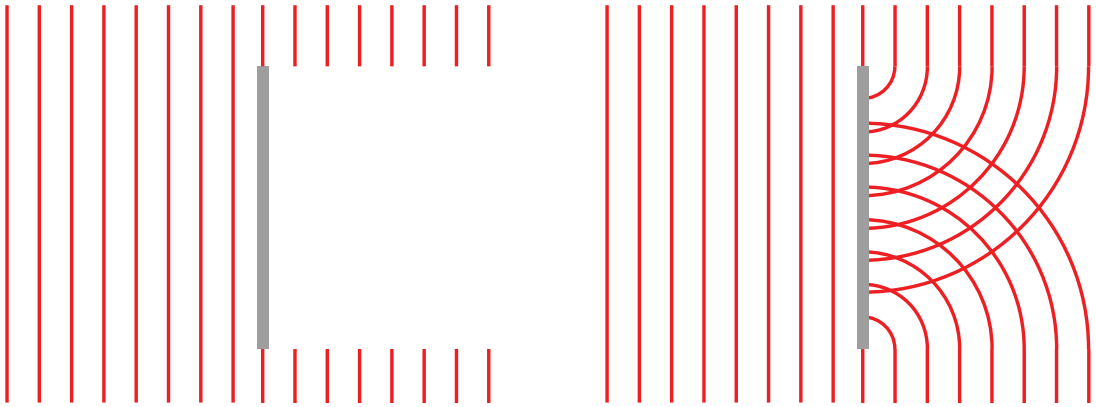

(a) (b)

Figure 3.5: Schematic of Huygens's principle. (a) Schematic of the projection of a shadow where diffraction isn't considered. (b) Schematic of a diffraction phenomenon according to Huygens's principle. The red lines represent wave-fronts and the grey area represents an obstacle.

This phenomenon is explained by Huygens's principle [26]. This principle states that in wave propagation, each point of a wave-front acts as a point source, and the overlap of the infinite wavelets results in the wave-front in propagation.

Different waves originating on the edges of the obstacle will intercept and interfere. In some areas each wave will have travelled unequal lengths, creating a phase difference. The interference of these waves will generate an interference pattern.

The path length of the radiation can be calculated [27] according to the following expression

$$L(\theta) = \frac{(1 - C(v) - S(v))^2 + (C(v) - S(v))^2}{4}, \tag{3.30}$$

where θ represents the diffraction angle as shown in the figure 3.6, $C(v)$ and $S(v)$ are the Fresnel integrals given by

$$C(v) = \int_0^v \cos\left(\frac{\pi s^2}{2}\right) ds, \tag{3.31}$$

$$S(v) = \int_0^v \sin\left(\frac{\pi s^2}{2}\right) ds, \tag{3.32}$$

and v represents Fresnel's parameter given by

$$v = h\sqrt{\frac{2}{\lambda}\left(\frac{1}{d_1} + \frac{1}{d_2}\right)}, \tag{3.33}$$

where h is the effective height of the obstacle (as shown in figure 3.6), and λ the wavelength. The direct distance x can be determined by the law of cosines

$$x = \sqrt{d_2^2 + d_1^2 - 2d_1 d_2 \cos(\pi - \theta)}. \tag{3.34}$$

From x, the angle α can be derived

$$\alpha = \cos^{-1}\left(\frac{d_1^2 + x^2 - d_1^2}{2xd_1}\right), \tag{3.35}$$

and so, the object's height can be determined

$$h = d_1 \tan(\alpha). \tag{3.36}$$

While being diffracted by the edges, the waves also suffer attenuation. This is caused by the finite thickness of the object. The wider the obstacle is compared to the wavelength, the more energy will be absorbed. Attenuation also depends on the material, in the sense that it is higher for materials that have a lower permeability to that wavelength. In order to analytically calculate the impact of this effect, complex calculations dependant on the edge's shape would be necessary [28].

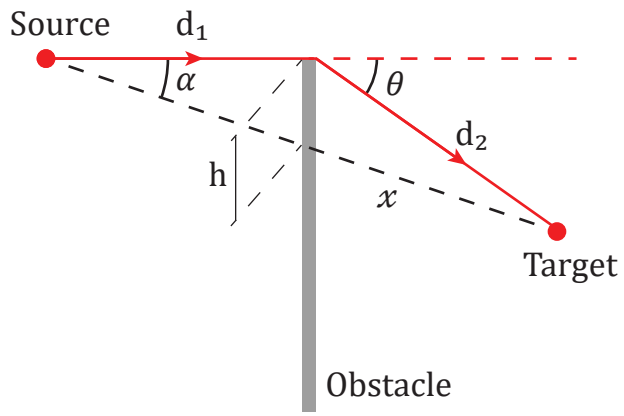

Figure 3.6: *Knife-edge* diffraction schematic.

3.3 Deconvolution

In an ideal system, a captured image would be identical to the object. However, real systems deform the captured information. This deformation can be caused by imperfections in the lenses, by the fact that the aperture is not punctual, by nonuniform sensitivity in the sensor, etc. Fortunately, the deformation can be compensated in post-processing by running a deconvolution filter through the data. A common method resorts to the determination of the *point spread function* in order to restore the image.

3.3.1 *Point Spread Function*

The deformation a system applies can be defined by the equation [19]

$$g[m,n] = h[m,n] * f[m,n], \tag{3.37}$$

where $[m,n]$ are the matrix's dimensions, g represents the acquired image, f the original image and h the deformation function or *point spread function*. On the frequency domain, i.e. the Fourier space, the problem is equivalent to

$$G[u,v] = H[u,v]F[u,v]. \tag{3.38}$$

On this domain, if the *point spread function* H is known, the image can be restored through the following division

$$\hat{F}[u,v] = \frac{G[u,v]}{H[u,v]}. \tag{3.39}$$

It is relevant to state that $\hat{F}$ can be different from F. This occurs when the function H has frequencies for which it takes the value zero. In this case, the division (3.39) would be invalid and these points would represent information loss in the system. In order for the operation to still be solvable, it is common to replace the zeros with low values for these frequencies.

Another factor that can complicate the process is the presence of noise. If a function of noise w is added to the equation (3.37)

$$g[m,n] = h[m,n] * f[m,n] + w[m,n], \tag{3.40}$$

then, the equation (3.39) becomes

$$\hat{F}[u,v] = \frac{G[u,v]}{H[u,v]} = \frac{H[u,v]F[u,v]}{H[u,v]} + \frac{W[u,v]}{H[u,v]}. \tag{3.41}$$

In this situation, the noise can be amplified leading to a processed image with more of it. To combat this problem, noise filters may be applied to the image before the deconvolution is performed.

Chapter 4

Experimental Procedure

4.1 Setup of the CW THz Tests

The system used in this work is comprised of a terahertz radiation source and detector mounted to a *computer numerical control* (CNC) table. An acquisition board is attached to the detector and linked to a computer that both assembles the data and controls the table.

4.1.1 Movement Control and Acquisition

The scanner has a three orthogonal axis positioning system over a volume of 2760×1960×2000 mm with a maximum resolution of 0.01 mm in the X and Y axis and 0.001 mm in the Z axis. For transmission imaging, the parts were positioned as shown in figure 4.1. The dimensions A through D will be referred to throughout the rest of this work.

In order to register the voltage produced by the detector, an acquisition board is connected to it. This board links to a computer where a *LabView* code compiles the collected data, allowing it to then be exported. This *LabView* program also builds the g-code used by the table, where the dimensions, resolution and speed of the scan are set. To ensure synchronisation between movement and measurement, the triggering of the acquisition is done by a digital signal sent by the table directly to the acquisition board. The scans are performed in a raster pattern, i.e. back and forward every other line, and the *LabView* code rearranges the data allowing the scan to be twice as fast. However, because of the limited motor acceleration, an offset still occurs between every other line since the motors take some time to reach full speed while the board dictates a constant sampling rate. This issue is addressed later on, in the signal processing section 4.2.1.

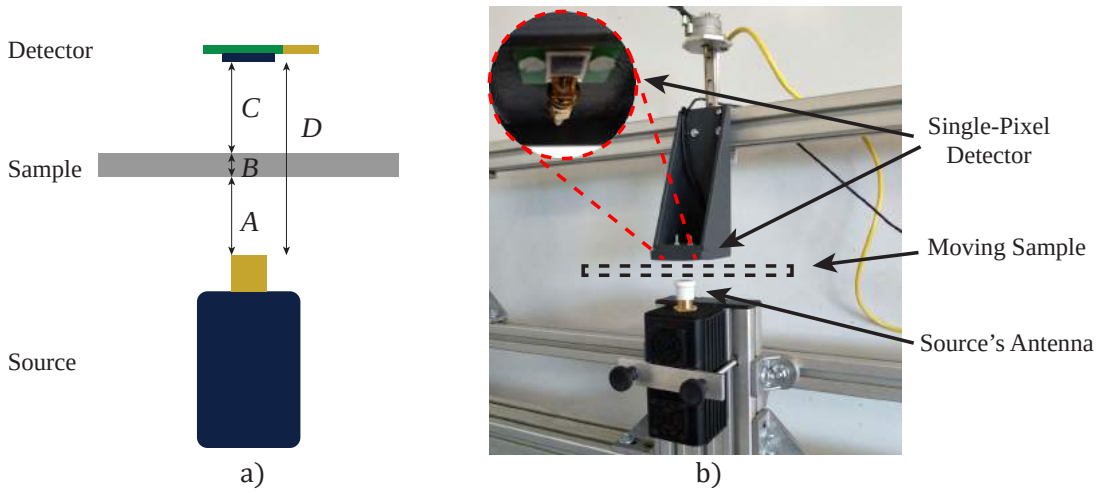

Figure 4.1: Setup used of continuous wave terahertz imaging in transmission mode. (a) Schematic representation of the setup. b) Picture with the dimensions referred to in this work. A video of the system in operation can be found **here**.

4.1.2 The Detector

The detector used was produced by the company *TeraSense*. It is sensitive to radiation between 50 GHz and 0.7 THz, with a typical response of 10 V per Watt of incident radiation. The detection area is a 7×7 mm square that can be seen as the dark square in figure 4.2a. The detector also has a fast response time of 1 microsecond, which allows for very fast scans at theoretical frequencies of 100 kHz without the response overlapping between measurements. As consequence, the limiting factor in scanning speed will usually be the mechanical speed. At the time these experiments were performed, 5G networks have not yet been implemented near the facilities, so no interference is expected. However, since this technology aims at frequency bands up to 100 GHz [29] some form of shielding, or a lock-in amplifier, might be necessary in the future.

4.1.3 The Source

The radiation source (figure 4.2b) was also acquired to *TeraSense*. It is marketed to produce a 80 mW beam of 0.1 THz radiation. However, the frequency was found to differ slightly from this value as it is explained in subsection 5.1. The frequency of 0.1 THz was picked as these sources tend to be more affordable than their higher frequency counterparts. This makes it so a higher power source can be acquired at a similar cost, which while having a worse resolution, will provide a better SNR. Additionally, as it can be seen in [25], 0.1 THz suffers lower attenuation in most materials when compared to higher frequencies, which further helps to mitigate the problem of low SNRs when imaging thicker objects. The beam has a starting diameter of 7 mm and a total divergence angle of 18°. The full characterisation of the source, as provided by the manufacturer, can be found in the appendix A.

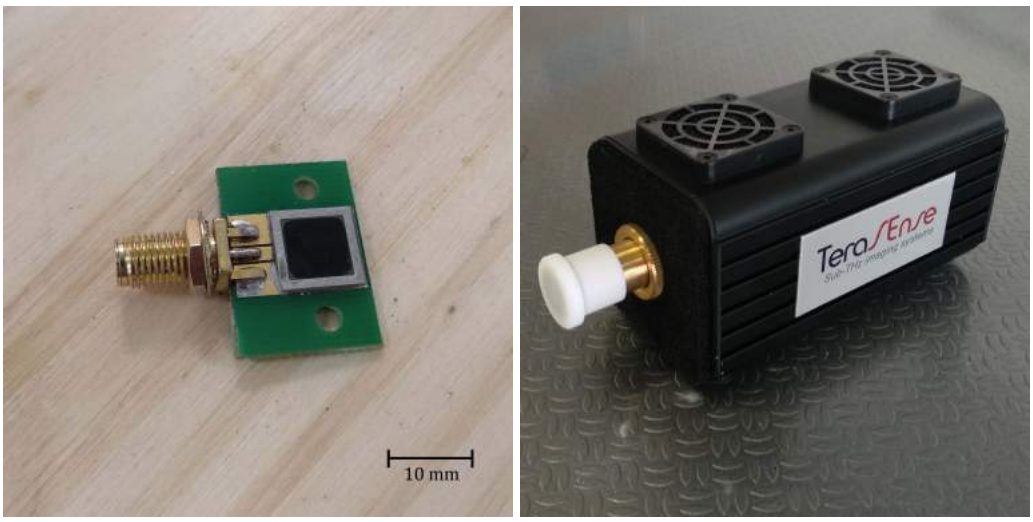

(a) (b)

Figure 4.2: Images of the source and detector. (a) Picture of the detector used. (b) Picture of the source used.

In order to better understand the images produced by the system, it was important to characterise the beam emitted by the source. To do so, a set of scans were performed involving only the detector and source. The source was installed to a fixed part of the table, while the detector was attached to the moving actuator. And so, C-scans were performed by moving the detector in a plane perpendicular to the beam ($x \circ y$) at different heights (z), as shown in figure 4.3.

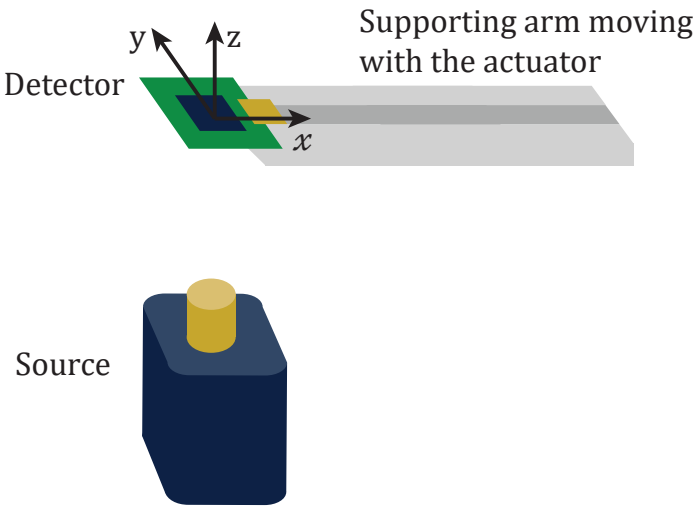

Figure 4.3: Schematic representation of the setup used to characterise the source.

These scans were done with a step size of 0.2 mm in the x and y directions. Because the step size is considerably smaller than the size of the detector (7 mm of width), the produced images would be convoluted. To restore the image to a more accurate state, the a Richardson-Lucy deconvolution filter [30] was applied using a 35 pixel wide, uniform square as the PSF. This function was chosen since at a 0.2 mm resolution this is the shape a 7×7 mm detector takes. The results were as shown in figure 4.4.

On the images where the detector was closer to the source, multiple peaks appear around the centre of the beam. It is suspected that these were caused by the proximity of the detector itself, where it reflected some of the waves and created an interference pattern.

Another set of scans were done where the detector moved in a plane parallel to the propagation of the beam. The resulting scan is shown in figure 4.5. In this image, the dispersion of the beam can be observed as well as a wave pattern. Upon closer inspection (figure 4.6), the frequency of the wave pattern appears close to expected value, i.e. half of the radiation frequency. By taking an average of the distance between peaks and multiplying it by the resolution of the scan, we arrive at (1.60 ± 0.01) mm which corresponds to half the wavelength. Inverting this value and multiplying by the speed of light, the frequency of (94.3 ± 0.06) GHz is revealed, which differs slightly from the 100 GHz announced by the supplier. This deviation is studied further on in subsection 5.1.

Figure 4.6 shows that this oscillating phenomenon could potentially have a strong impact in the images. The effect was found to be a form of Fabry-Perot interference and is discussed in detail in section 5.1. This plot was also useful to analyse the beam dispersion. A exponential function, in the form $I = I_0 e^{(ax)}$, was fitted to the medium points of the wave resulting in $I_0 = 15.7$ mV and $a = -2.1 \times 10^{-5}$ (with x in mm).

To better analyse this effect, a support for the detector was built where the detector is attached to a carriage that is moved, in the z direction, by a stepper motor as it is shown in figure 4.7. The M3 lead screw that moves the carriage has a pitch of 0.5 mm and the motor does 48 steps per revolution. This way, through the *LabView* program the detector height can be precisely controlled with a precision of (0.5 mm) /48 = 10.42 µm.

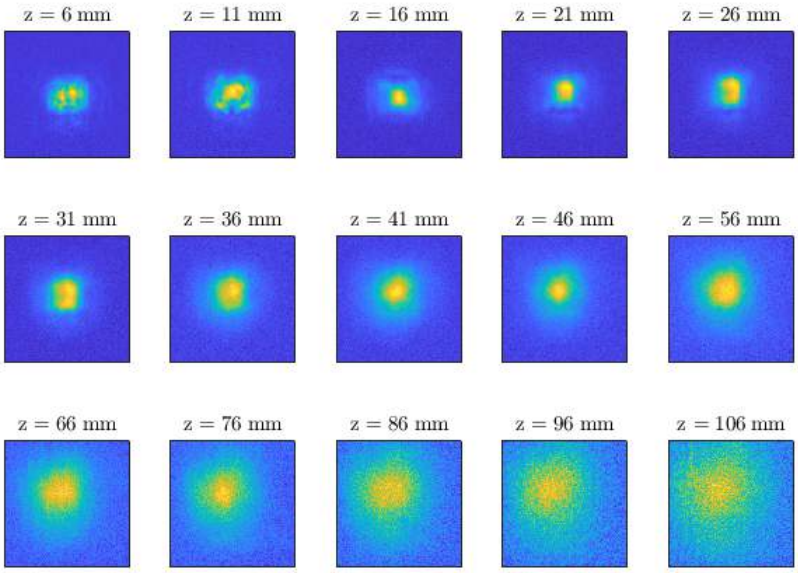

(a)

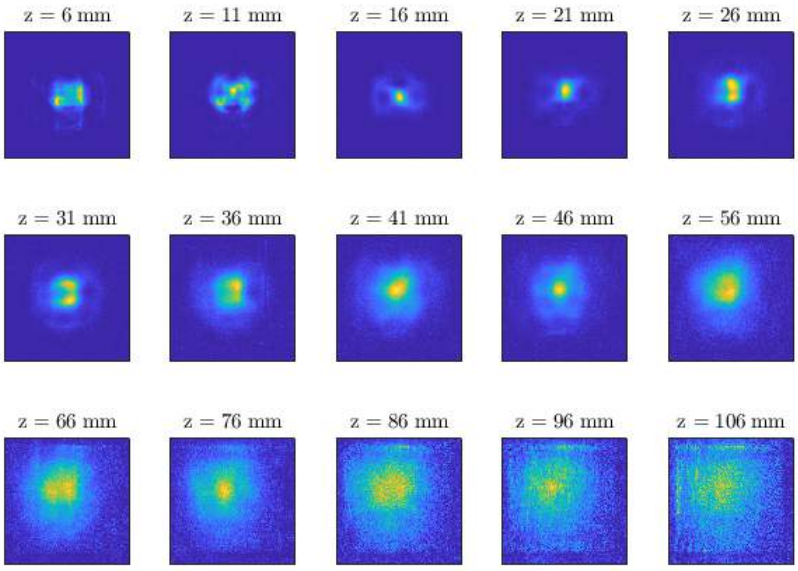

(b)

Figure 4.4: Images of the scans of the radiation source at different heights z. Figure (a) shows the original data before fixing deformation and deconvolution and figure (b) shows the results after this processing was performed. It is important to note that each individual image has a different colour scale to ease the visibility of the shape. A more accurate image with normalised colour scales can be found in the appendix B.

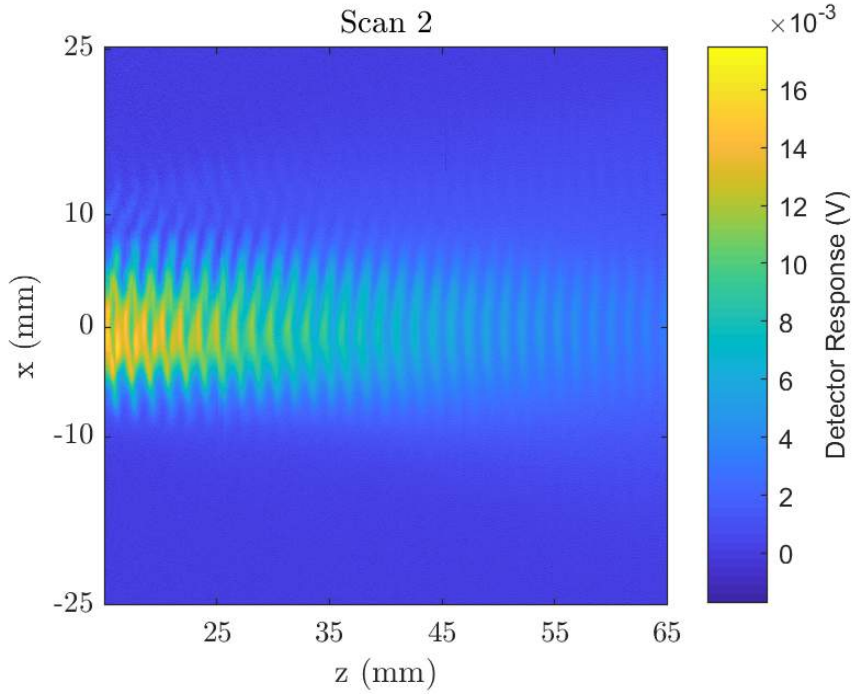

Figure 4.5: Scan parallel to the radiation beam. The source was located at the left side of the image projecting radiation horizontally.

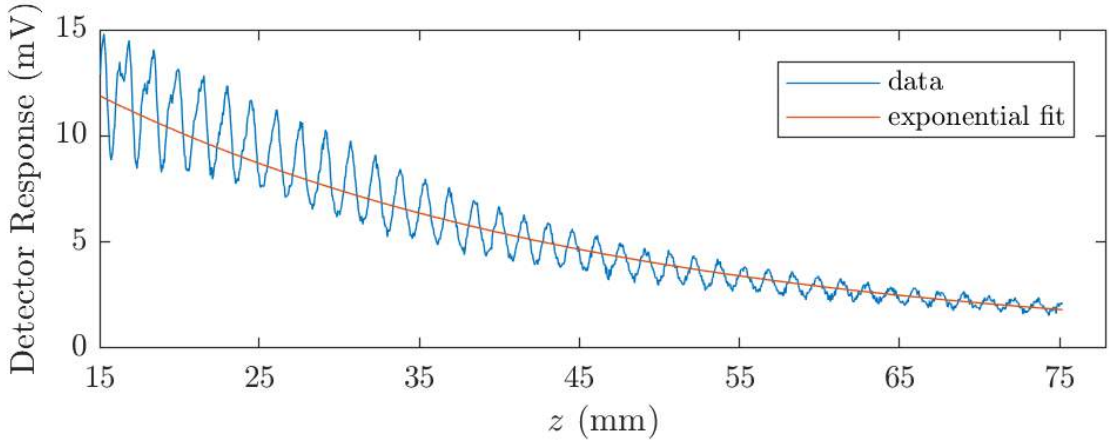

Figure 4.6: Central line extracted from the matrix in figure 4.5. The fit was and exponential function in the form $I = I_0 e^{(ax)}$, fitted to the medium points of the wave resulting in $I_0 = 15.7$ mV and $a = -2.1 \times 10^{-5}$ (with x in mm).

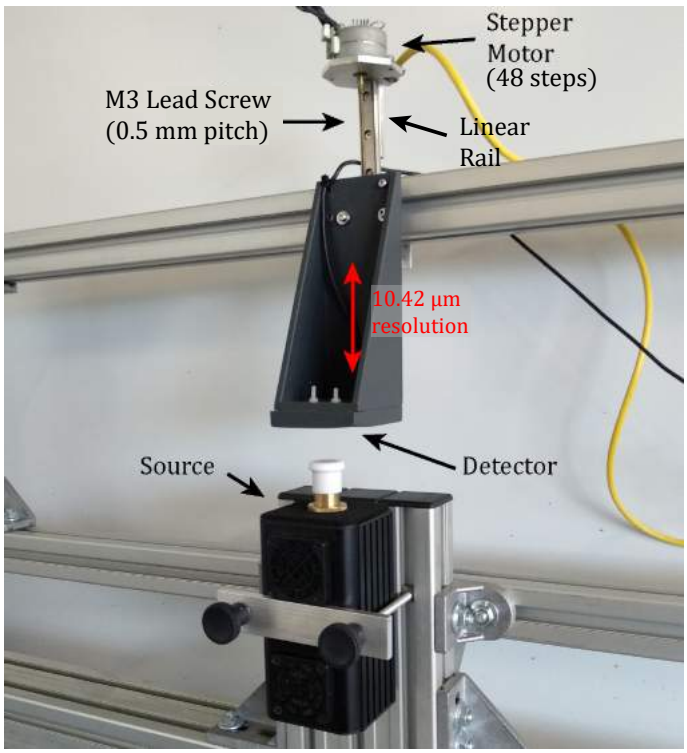

Figure 4.7: Picture of the stepper motor that moves the detector.

4.2 Image Processing

4.2.1 Fixing Measurement Deformation

As mentioned previously, because of the limited acceleration of the stepper motors and the imposed constant sampling rate of the acquisition board, when the scan is done in a raster pattern, there is a slight offset every other line of the image matrix. This problem could be easily fixed by scanning all lines in the same direction, but that would double the acquisition time, so instead, the problem was fixed in post-processing by a *MATLAB*^{TM} script. The solution consists in shifting every other column of the image matrix by a few pixels depending on the resolution of the scan. This results in the elimination of a few lines on the top and bottom of the image, but it effectively restores the results as it can be seen in figure 4.8. A different amount of pixels needs to be shifted depending on the resolution and the speed of the scan, being that finer resolutions and faster speeds require larger shifts. All scans showed in this work have had this correction applied.

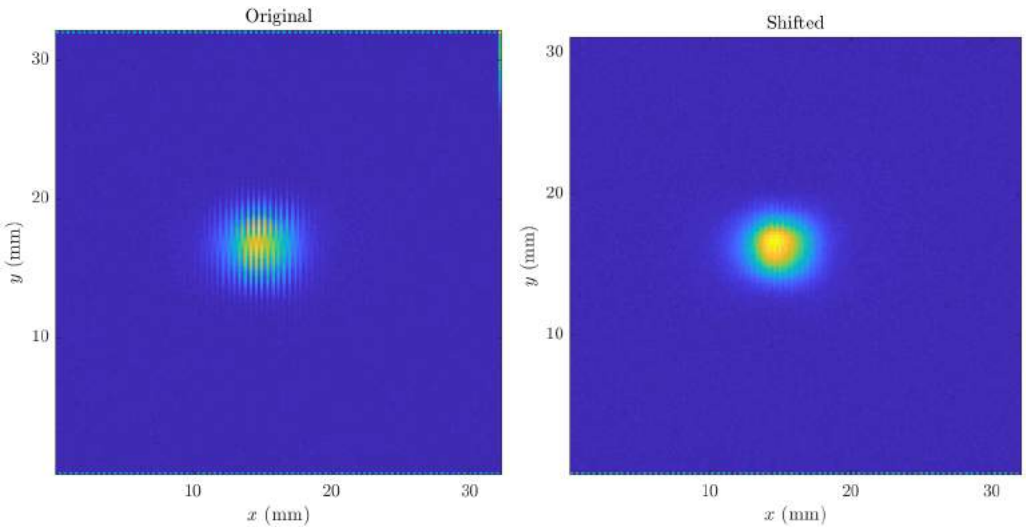

(a) (b)

Figure 4.8: Images of a scan of a 5 mm hole on a stainless steel sheet. Image (a) is the original collected data and (b) is after fixing the shift caused by motor acceleration.

4.2.2 Deconvolution

Previously, when addressing the characterisation of the source, a deconvolution method was applied using a simple point spread function. However, when scanning objects, the scan is performed so that the source and detector stay fixed in relation to each other while the sample moves between them, like shown in figure 4.9. In this scenario, because the radiation from the source does not hit the detector uniformly, the shape of the point spread function is not trivial.

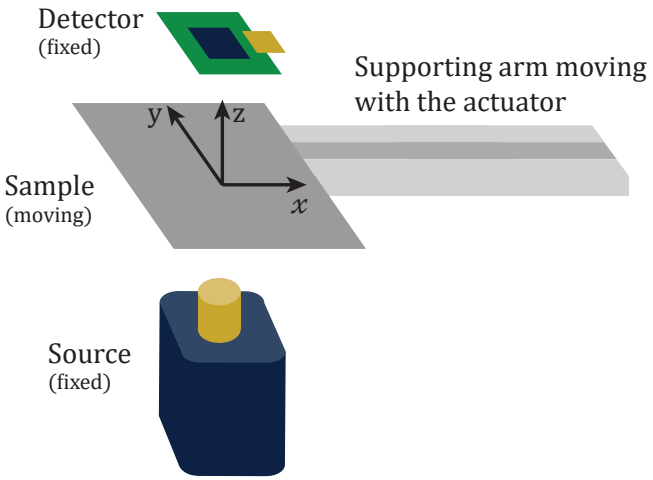

Figure 4.9: Setup used for sample imaging.

Deconvolution was experimented with the Richardson-Lucy, blind deconvolution and Wiener filter methods [30]–[32]. The latter provided the best results. Each method was tested with an assortment of different PSF shapes, and for each shape a range of parameters was tested. The best results were obtained with Wiener filter deconvolution using a Gaussian shape. In figure 4.10 a comparison is shown between the original acquired image and the processed one. The imaged object is a piece of scrap zirconia, with a thickness of 10 mm, and was picked as a benchmark due to is variety of shapes and features. It can be observed how the deconvolution not only removed image artefacts, but also resolved the sharp edges on the left border of the object.

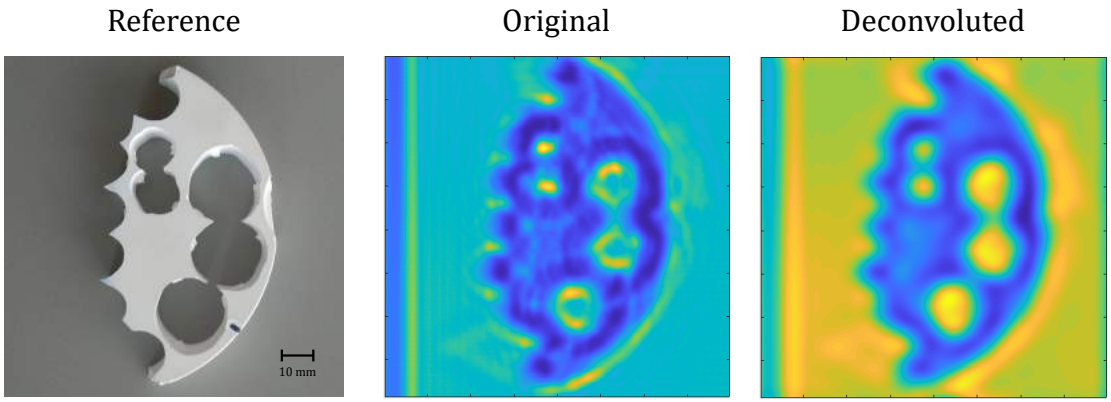

Figure 4.10: Comparison between a reference picture, the original data and a deconvoluted image. The deconvolution produces an image more faithful to the original, where the sharp vertices on the left can now be discerned. The piece is roughly 9 cm long and was scanned at a 0.25 mm resolution.

Due to the nature of the scan, the point spread function will depend on the resolution the image is taken at. However, this factor can be easily adjusted by scaling the PSF inversely by a factor inverse to the change of resolution. Unlike the pixel-shift mentioned in the last section, deconvolution was not applied to the rest of the images presented in this work, as to preserve accuracy in relation to the acquired data.

In the future the point spread function could be further studied to achieve better results. Alternatively, with machine learning, an algorithm such as a *neural network* could be trained to reconstitute these images.

Chapter 5

Results and Discussion

5.1 Fabry-Perot Interference

Preliminary tests showed high amplitude gradients as a background of some of the scans. This effect seemed more prevalent when the sample was tilted or bent, and in the most extreme cases the gradient became a wave pattern.
To better understand the effect, a set of scans were done where either the sample or the detector were moved vertically (varying the dimensions C and D from figure 4.1).

The results (figure 5.1) show an oscillation that had a consistent period independent of the thickness or material of the sample. This period also coincided with the one measured when characterising the source. These results, along with an analysis of the geometry of the experiment, seemed to point towards a phenomenon of Fabry-Perot interference. To validate this hypothesis, a MATLAB^{TM} (appendix C) program was written based on the equation 3.26. A situation with a sample would have 4 interfaces: Source-Air; Air-Sample; Sample-Air; Air-Detector, as shown in figure 5.2. This corresponds to the situation shown in figure 3.2, three times "in series". The program calculates the results by multiplying the equation three times, each with their corresponding parameters. This approach ignores attenuation and re-reflections between "interferometers" and thus the results are merely qualitative. Nonetheless, by using this method to reproduce the scan with glass shown in figure 5.1, the results from figure 5.3 were obtained, which qualitatively, seem to agree with the experiment.

To perform the aforementioned calculations, the values for the refractive indexes of the source and detector were needed. However, these parts have odd shapes that would make the calculation of the reflectivitty unfeasible. As an approximation, the dispersion caused by shape was combined with the refractive index of the materials to assume a virtual value of reflectivitty. These values were numerically determined so that

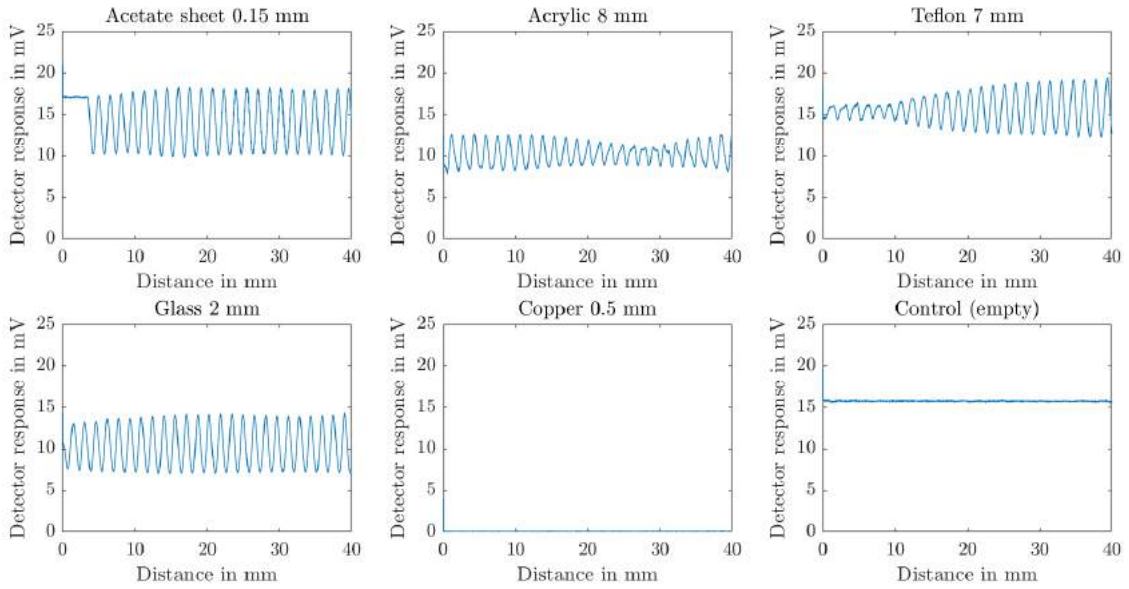

Figure 5.1: Results of vertical scans using different samples. All show a similar period of 1.6 mm.

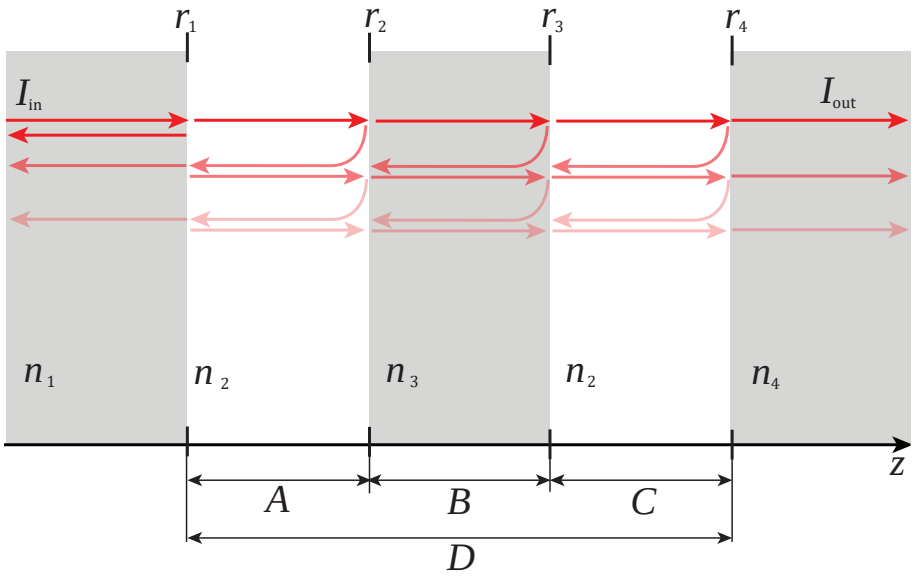

Figure 5.2: Schematic of interference in 4 interfaces. The dimensions are as shown in figure 4.1 and as such, the mediums n_1 to n_4 correspond to the source, air, sample and the detector respectively.

a calculation of the scan performed in figure 4.6 would have the most faithful results in terms of the relation between the amplitude of oscillation and the mean value.

According to this equation, and the ones used further on, the oscillation in these scans should have half the wavelength of the radiation. However, through MATLAB^{TM}, in the experimental data the distance between peaks was measured to be 1.6 mm instead of

the expected 1.5 mm. This value was consistent for all measurements taken throughout this work. As such, it was concluded that the source emits 94 GHz radiation instead of the advertised 100 GHz. From here on out, when the frequency and wavelength of the radiation are mentioned, it is referring to 94 GHz and 3.2 mm respectively.

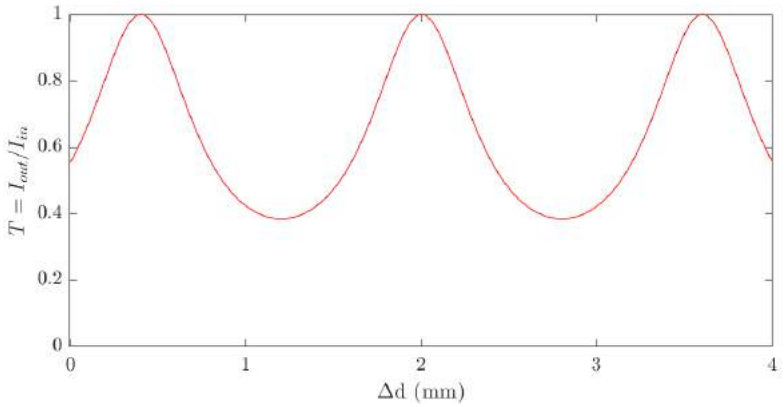

Figure 5.3: Results of a calculation of the transmitted intensity when a 2 mm glass panel is moved vertically in the scanner.

These results now raise the question of how important the placement of the sample and detector is for imaging. To analyse the impact of these distances, a set of acquisitions were performed where both the height of the detector (C) and sample (A) travelled independently, a span of 5 mm at steps of 0.1 mm each. This was done by raising the sample in increments of 0.1 mm, effectively raising A while lowering C, and after it travelled 5 mm, the detector would then be raised 0.1 mm until this one too, had travelled 5 mm. A measurement was taken for each combination of both heights which produced 2500 values. Figure 5.4 shows the results of these scans where the axis represent the variation in width of the cavities shown in figure 4.1 and 5.2.

Using the aforementioned equation in a MATLAB^{TM} script, these scans were reproduced resulting in the image presented in figure 5.5. These results differed significantly form the ones obtained experimentally. As it was mentioned previously, by multiplying the equation this approach considered that the three cavities were independent. It was thus hypothesised that this approximation was the culprit of the disparity between results.

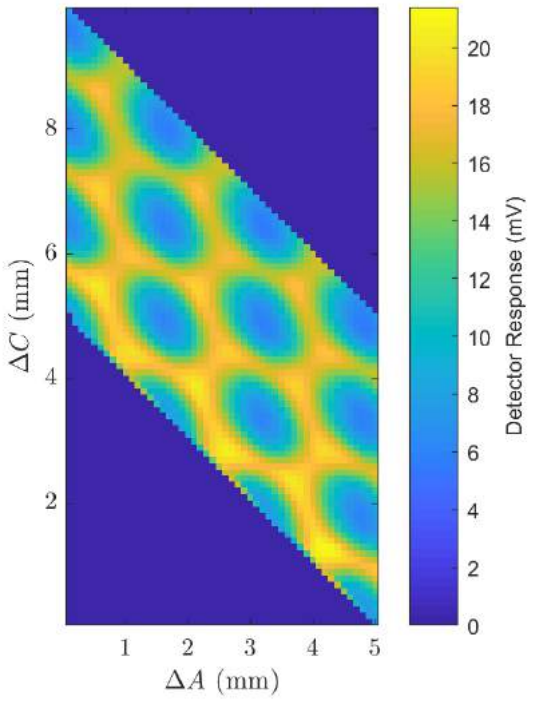

Figure 5.4: Experimental results of a scan where the lengths of the cavities are varied. The axis variations in the length of the cavities corresponding to the dimensions labelled in figure 4.1 and 5.2. The two dark areas correspond to positions that were not measured. An animated GIF, that better illustrates the scanning movement can be found **here**.

To address this issue, a matrix method was employed as described in [33]. Here, the resulting expression for transmitted intensity T is:

$$T = \tau\tau^*, \tag{5.1}$$

where τ^* is the conjugate of τ and:

$$\begin{aligned}
\tau = \tau_1\tau_2\tau_3\tau_4/\{&exp[j(-\phi_1-\phi_2-\phi_3)] \\
&+ r_1r_2\ exp[j(+\phi_1-\phi_2-\phi_3)] \\
&+ r_2r_3\ exp[j(-\phi_1+\phi_2-\phi_3)] \\
&+ r_1r_3\ exp[j(+\phi_1+\phi_2-\phi_3)] \\
&+ r_3r_4\ exp[j(-\phi_1-\phi_2+\phi_3)] \\
&+ r_1r_2r_3r_4\ exp[j(+\phi_1-\phi_2+\phi_3)] \\
&+ r_2r_4\ exp[j(-\phi_1+\phi_2+\phi_3)] \\
&+ r_1r_4\ exp[j(+\phi_1+\phi_2+\phi_3)]\},
\end{aligned} \tag{5.2}$$

where τ_i is the transmissivity given by $\tau_i = \sqrt{1-r_i^2}$, j is the imaginary identity and ϕ_i [rad] is the phase length of each cavity given by

$$\phi_i = \frac{2\pi L_i n_i}{\lambda}. \tag{5.3}$$

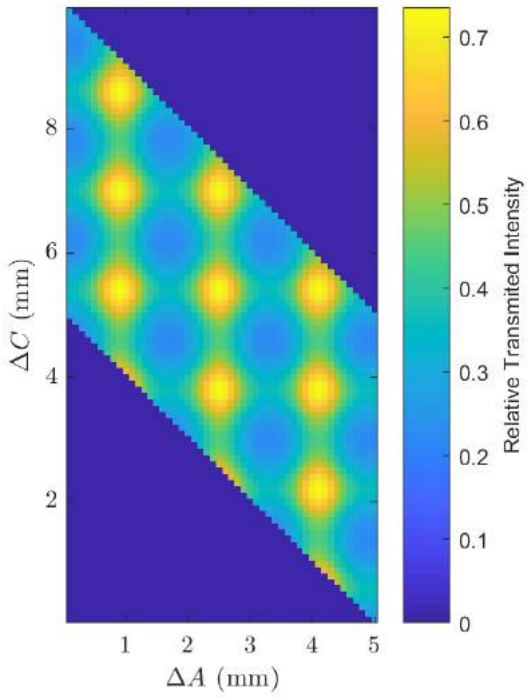

Figure 5.5: Results of a calculation simulating the scan performed in figure 5.4. The axis variations in the length of the cavities corresponding to the dimensions labelled in figure. 4.1 and 5.2.

By implementing this equation in a MATLAB^{TM} script (found in the appendix C), the results shown in figure 5.6 were produced. While closer, the plot differs from experimentation nonetheless.

Both equations used previously considered lossless reflections and propagation through the medium. It was thus hypothesised that taking the energy losses into account could produce more accurate results. As such, an attenuation coefficient was attributed to each cavity. This coefficient is a virtual value that encompassed both the attenuation by the reflections and the dispersion through the medium. Since the variations in size of each cavity are much smaller than the sizes themselves, an approximation was made where these coefficients are independent from changes in cavity size.

Each component of equation (5.2) was multiplied by a attenuation coefficient (at_i) according to the cavities each component passed through. Note that $(at_1)(at_2)(at_3)$ was omitted from each component since it is common to all components, so it would not make a qualitative difference. Equation (5.2) thus becomes:

$$
\begin{aligned}
\tau = \tau_1\tau_2\tau_3\tau_4/\{&exp[j(-\phi_1-\phi_2-\phi_3)] \\
&+ (at_1)^2\, r_1r_2\, exp[j(+\phi_1-\phi_2-\phi_3)] \\
&+ (at_2)^2\, r_2r_3\, exp[j(-\phi_1+\phi_2-\phi_3)] \\
&+ (at_1)^2(at_2)^2\, r_1r_3\, exp[j(+\phi_1+\phi_2-\phi_3)] \\
&+ (at_3)^2\, r_3r_4\, exp[j(-\phi_1-\phi_2+\phi_3)] \\
&+ (at_1)^2(at_2)^4(at_3)^2\, r_1r_2r_3r_4\, exp[j(+\phi_1-\phi_2+\phi_3)] \\
&+ (at_2)^2(at_3)^2\, r_2r_4\, exp[j(-\phi_1+\phi_2+\phi_3)] \\
&+ (at_1)^2(at_2)^2(at_3)^2\, r_1r_4\, exp[j(+\phi_1+\phi_2+\phi_3)]\}.
\end{aligned}
\tag{5.4}
$$

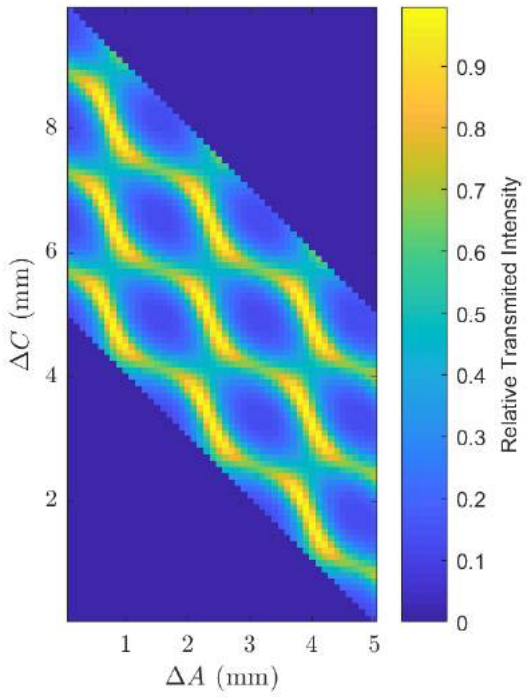

Figure 5.6: Results of a calculation simulating the scan performed in figure 5.4 using equation (5.2). The axis variations in the length of the cavities corresponding to the dimensions labelled in figure 4.1.

Adding the attenuation coefficients to the MATLAB^{TM} script produces the plot shown in figure 5.7. These results show greater similarity with the ones obtained experimentally than any of the produced with previous methods.

With these results, it can be concluded that a analytical method was established that can predict the Fabry-Perot effect of a transmission system. Figure 5.8 shows a comparison between all attempted methods and the experimental results.

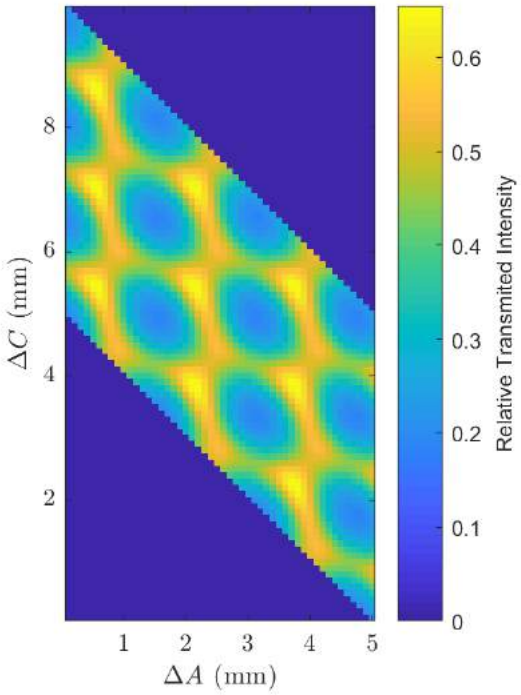

Figure 5.7: Results of a calculation simulating the scan performed in figure 5.4 using equation (5.4). The axis variations in the length of the cavities corresponding to the dimensions labelled in figure 4.1 and 5.2.

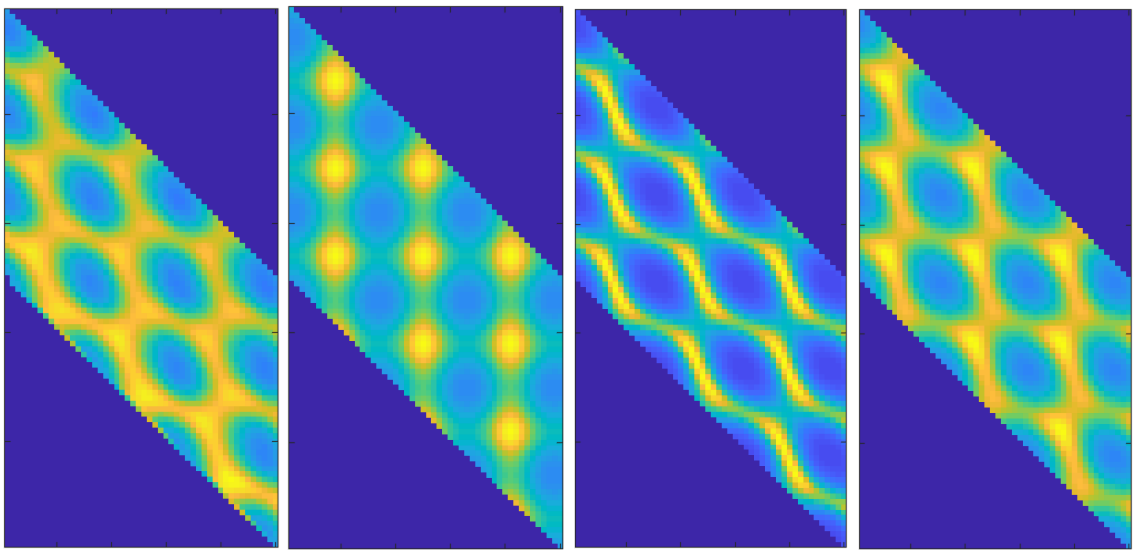

(a) (b) (c) (d)

Figure 5.8: Comparison between calculated results. (a) The experimental data. (b) Considering the cavities independent (equation (3.26)). (c) Considering interactions between cavities (equation (5.2)). (d) Considering the interactions and dispersive factors (equation (5.4)).

By raising only the sample, the most common movement throughout this work, the equation produces the output shown in figure 5.9.

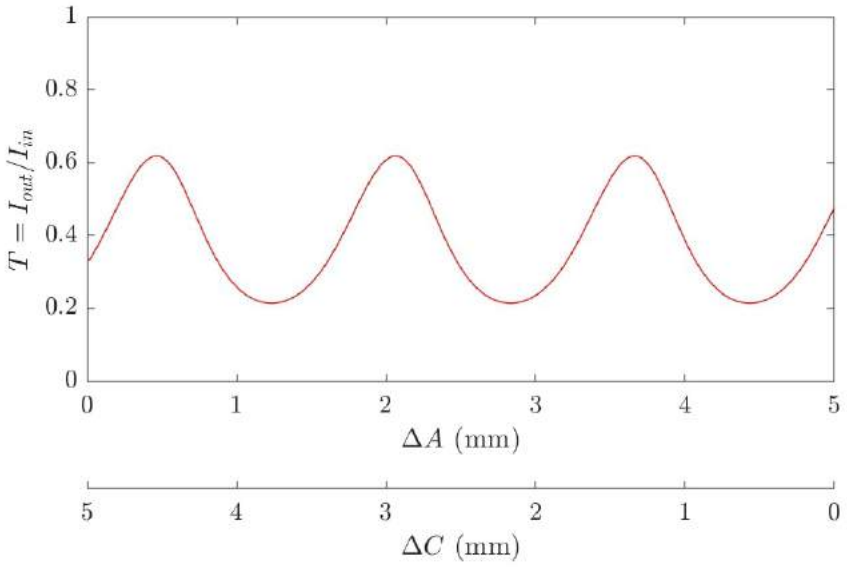

Figure 5.9: Plot using equation (5.4).

It is important to state that this approach assumes the components as planar objects. Through experiment it was observed that this approximation holds for surfaces with shapes that differ slightly from a plane, however for surfaces with a significant tilt or curvature this model is no longer valid. As such, the utility of this model focuses mainly on planar objects.

5.2 Contrast Analysis

The comprehension of the Fabry-Perot effect, described in the previous sub-section, now raises the question of what its impact is on the actual produced images. One known effect is the emergence of a background gradient when a sample is either tilted or bent. Figure 5.10 shows the effect on a polyactic acid (PLA) part with square, triangular and circular voids fully enclosed in the polymer, that is tilted and figure 5.11 shows a wave pattern on a similar sample that appears due to a slight bulge in its surface. These gradients raise the possibility for CW THz to be used as a metrology method. By understanding the pattern of the gradients small variations in thickness and tilt can be measured on a surface. Figure 5.11 is a prove of concept of this method. Since the pattern oscillates every half wavelength it is known that between two fringes there is a 1.6 mm difference in height or thickness. In a well studied and calibrated system where the transmissivity is known for a specific material and thickness, this could be used to measure irregularities in thickness or straightness.

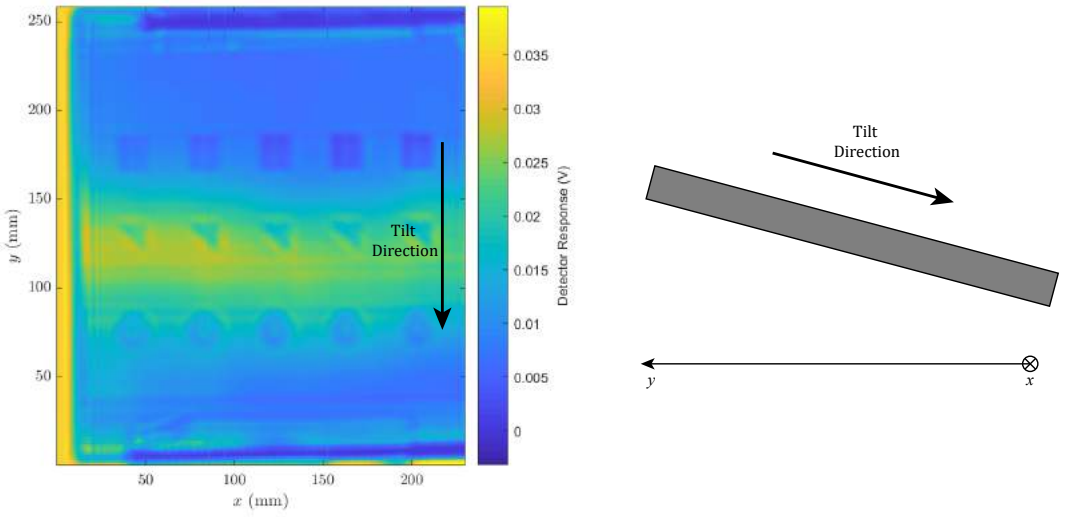

Figure 5.10: (a) Scan of a PLA sample with several artificial defects. A gradient is visible that varies in only one direction. This indicates that the sample was tilted. (b) A schematic representation of the tilt on the part (heavily exaggerated).

The Fabry-Perot effect does not solely affect the background, it also has an impact on the contrast of a defect. For an NDT application, the contrast is highly relevant as it is an indicator of how perceivable a defect will be.

As a first experiment, a 100 µm thick acetate sheet was laid with its border in the middle of an 8 mm thick acrylic plate, and a linear C-scan was taken centred on the border. Multiple linear C-scans were performed with the plate and detector set at different heights. As seen in figure 5.12, the transmitted intensity varies with the position of the sample in a

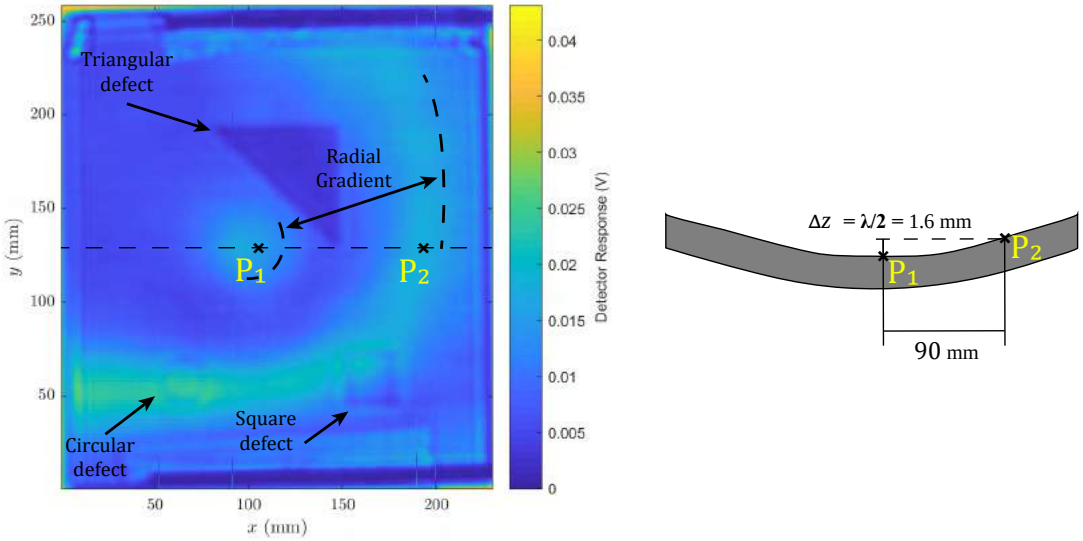

a) b)

Figure 5.11: (a) Scan of a PLA sample with three artificial defects, with a circular gradient pattern caused by the Fabry-Perot effect manifesting due to a deformation in the shape of the sample. The points P_1 and P_2 mark two peaks of the gradient, indicating that between these points there is a Δz of half the wavelength (1.6 mm). (b) A schematic representation of a cut through the dashed line, where the bulge of the sample is represented (heavily exaggerated).

periodic fashion. The height of the sample was picked either when the signal's amplitude was maximised, at the peak of the wave, or when the first derivative was maximised, at the middle point of the wave, outside of the acetate. As expected, the contrast (ΔV) was highest when both cavities were set to the medium point, where the slope is the highest, unlike the position that maximises signal, where the slope approaches zero. However, it is important to note that due to the periodicity of the effect, these results can only be expected in situations where the thickness of the defects is significantly smaller than half the wavelength.

A similar set of C-scans were also performed to a 5 mm thick PLA sample produced with extruded material by additive manufacturing, where a $20.0 \times 20.0 \times 0.5$ mm defect was purposely created (figure 5.13) which was meant to emulate a delamination or void. This defect was created in the printing possess and is fully encased within the polymer. The C-scans in figure 5.14 show the effect positioning can have on the contrast. In the scans between 0.8 mm and 1.4 mm, the square manifests as a shadow where the signal has a lower amplitude. On the contrary, the scans at 0.4 mm and 1.8 mm evidence the diffraction in the borders of the defect. It is also interesting to note that there is a periodicity between positions that show similar effects. This can be seen in the similarities of scans separated by 1.6 mm, such as: 0.0 mm and 1.6 mm, 0.2 mm and 1.8 mm, 0.4 mm and 2.0 mm, etc...

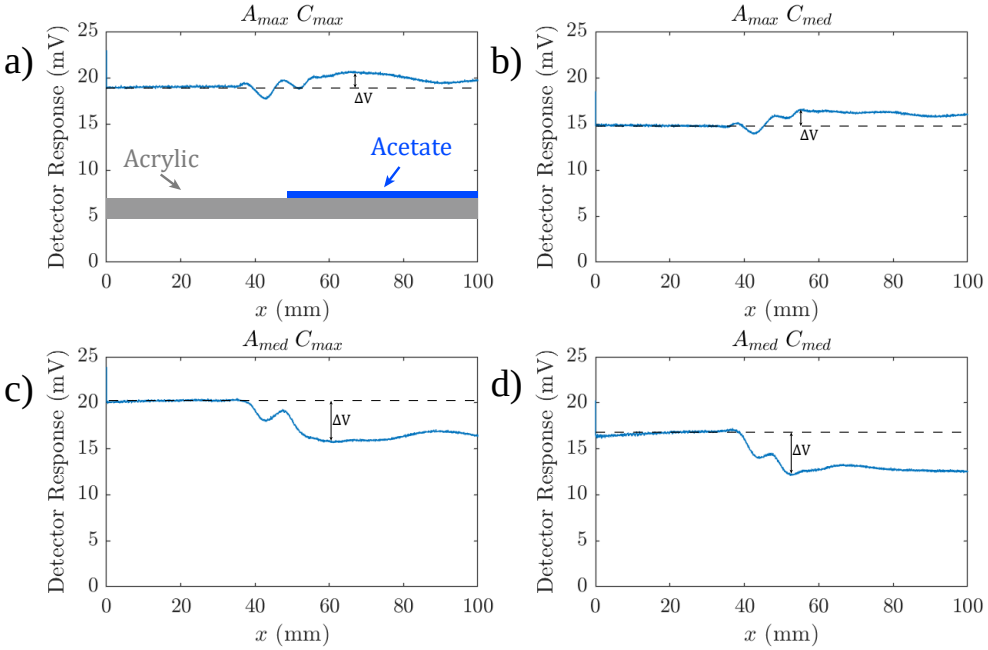

Figure 5.12: Results of a 100 mm linear C-scan of a 100 µm thick acetate sheet set on a 8.0 mm acrylic sheet. The positions were set so that the length of the cavities produced an amplitude that was either at a maximum or medium point (where the slope was highest) when measured without the acetate. In sub-figures a) thorough d), "A" and "C" represent the dimensions labelled to in figure 4.1, and "*max*" and "*med*" indicate if at that position the response was at a maximum or medium value, respectively.

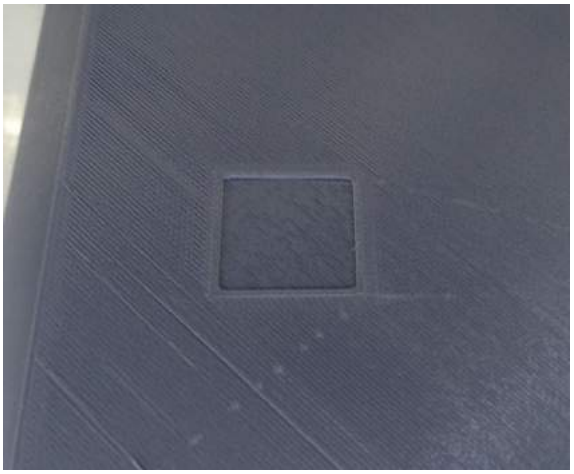

Figure 5.13: Picture of the $20.0 \times 20.0 \times 0.5$ mm artificial defect during the 3D printing of a 5 mm thick PLA part.

In a situation where there is a precise expected width of the test piece, the system could be set up to optimise to contrast the desired effect. Alternatively, if the dimensions are not precisely known or if both effects want to be observed, it is proposed that three or more scans are taken raising the sample 0.4 mm each time. This method of acquiring multiple C-scans ensures that there is at least one scan that favours each regime of interaction.

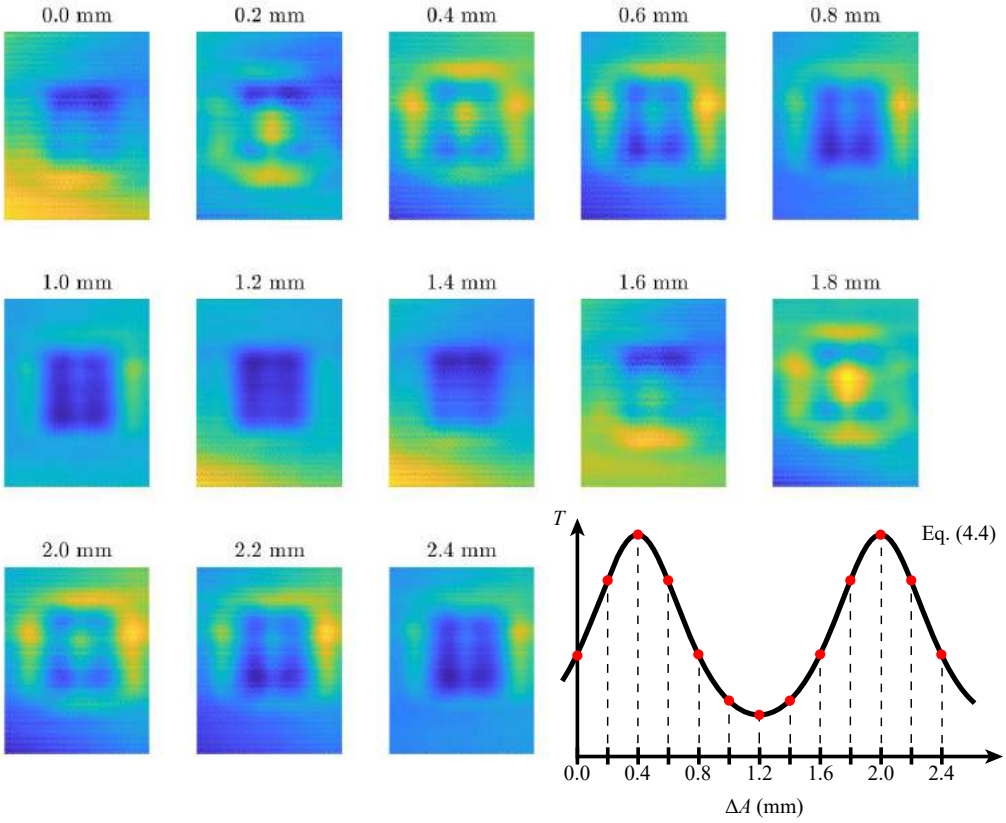

Figure 5.14: Results of several C-scan of a PLA sample done by positioning it at different heights A and C. The sample contained a $20 \times 20 \times 0.5$ mm square defect. On the bottom right, a graph represents qualitatively the signal's amplitude depending on the height of the sample. It is important to note that the detector height D was kept constant, and as a consequence, varying A causes C to vary inversely. On the bottom right, a graph shows the expected variation of the response when varying A, according to equations (5.1) and (5.4).

5.3 Enhancing the Resolution

As it was discussed previously, having a 7×7 mm detector limits the minimum resolution to about that size, since any finer details will get convoluted. It was proposed that by partially covering the sensitive area of the detector with a reflective material, a finer resolution would be possible at the exchange of measured amplitude, resulting in a lower SNR.

This approach was tested by placing an aluminium sheet on the detector with holes with different diameters punctured through (figure 5.15a). Also using aluminium sheet, a shape was glued to an acrylic plate with different features (figure 5.15b), as to better test the enhancements in resolution.

Diaphragms with 0.9 mm, 1.2 mm, 1.6 mm, 2.0 mm and 2.4 mm holes were tested. The best results were found for a hole with a diameter of 1.6 mm, as shown in figure 5.16. As expected, finer details such as the holes running through the middle, are now visible

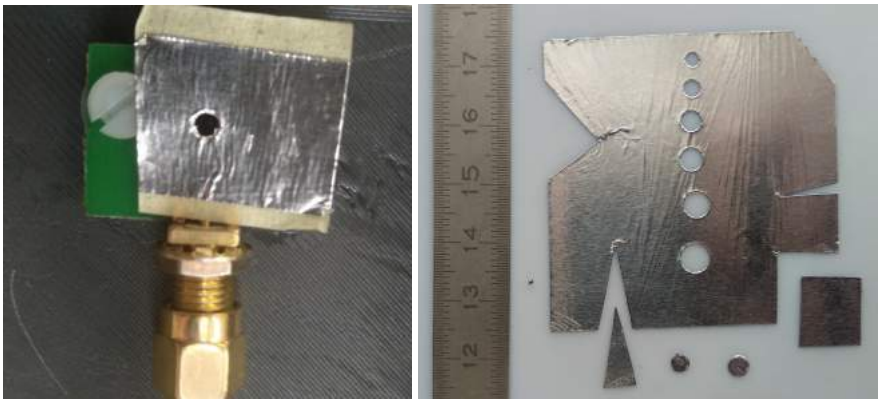

(a) (b)

Figure 5.15: Procedure for testing the diaphragms. (a) Diaphragm partially covering the detector. (b) Aluminium sheet sample used to test the resolution enhancement.

in higher detail. Also according to expectation, noise is now more visible. Smaller holes lowered the SNR to a point where it affected the perceptible shapes (figure 5.17). A apertures wider than 1.6 mm produced blurrier images. The 1.6 mm diameter hole being the optimal aperture is interesting since this dimension coincides with the half the wavelength of the radiation indicating that for apertures smaller that this ratio the transmitted radiation decreases intensity rapidly.

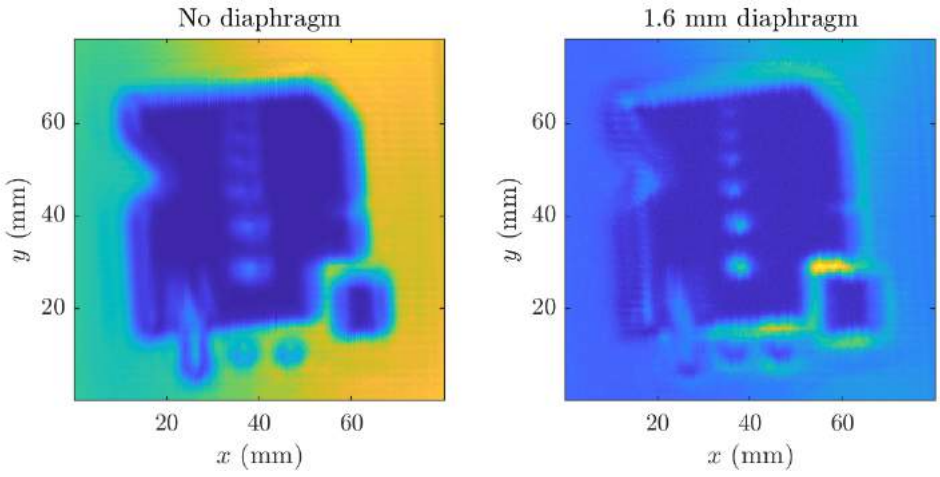

Figure 5.16: Comparison between an image with and without the 1.6 mm diaphragm.

As it was discussed previously, the positioning of the sample can have a great impact on the produced image. As such, the scan with the 1.6 mm diaphragm was performed at multiple heights. The results are presented in figure 5.18. Once again, each position highlights a different aspect of the sample being that some show the holes more precisely and some show a sharper border.

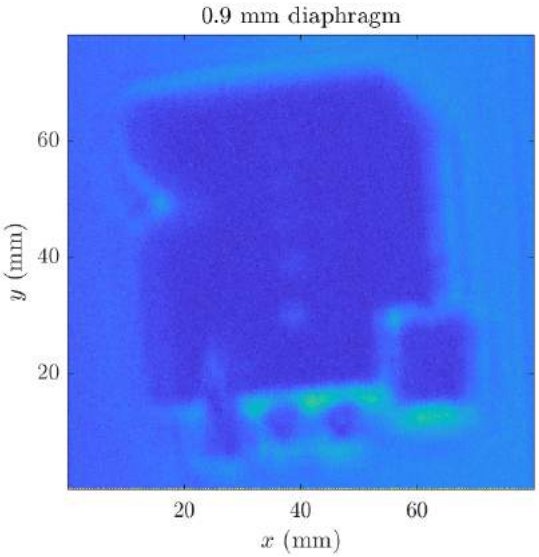

Figure 5.17: Results using a 0.9 mm diameter diaphragm.

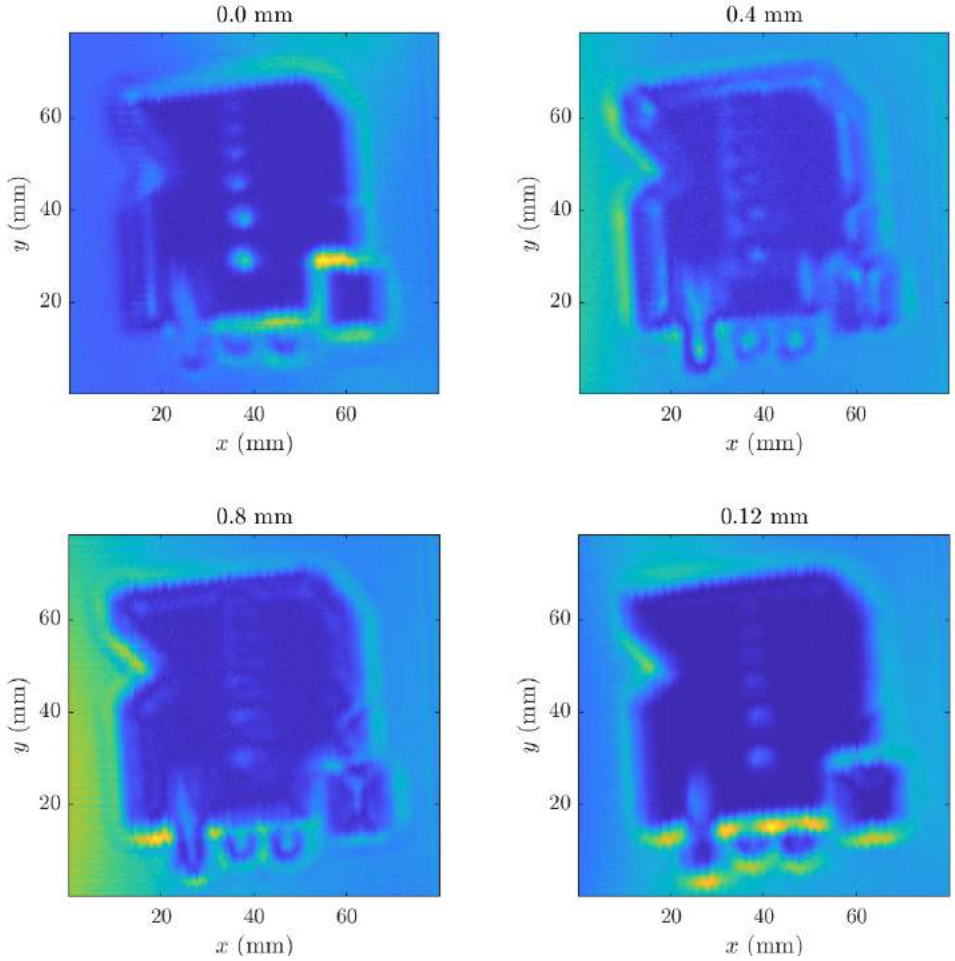

Figure 5.18: Results using a 1.6 mm diameter diaphragm at different A heights where 0.0 mm is an arbitrary position, and the values in the title represent a ΔA.

We can now conclude that if it is imperative to enhance the resolution, partially covering the detector could be a viable solution. If a more powerful terahertz source is used, the effect of the SNR reduction can be counteracted. Additionally, deconvolution could be applied to a image produced with a partially covered detector to enhance the resolution even further.

5.4 Analysis of Polymeric Samples

Along with ceramics, polymers are some of the materials of higher interest for terahertz imaging due to their low attenuation to these waves. Between the two, polymers are considerably easier to machine and parts can be produced by additive manufacturing with common 3D printers. Additive manufacturing also allows for the production of samples with defects that would otherwise not be machinable, such as voids and delaminations.

In this section, the analysis of several types of samples is shown along with a short discussion of the observations.

Figure 5.19 shows the scan of a PLA sample with a set 0.5 mm thick defects, with different geometric shapes simulating voids or delaminations similarly to what was done in figure 5.13. From left to right, the defects are positioned increasingly deeper in the part. All the shapes are clearly visible however, there is no distinction between the different depths. Additionally, as it was discussed previously, a gradient is visible indicating that the piece was tilted at the time of scanning.

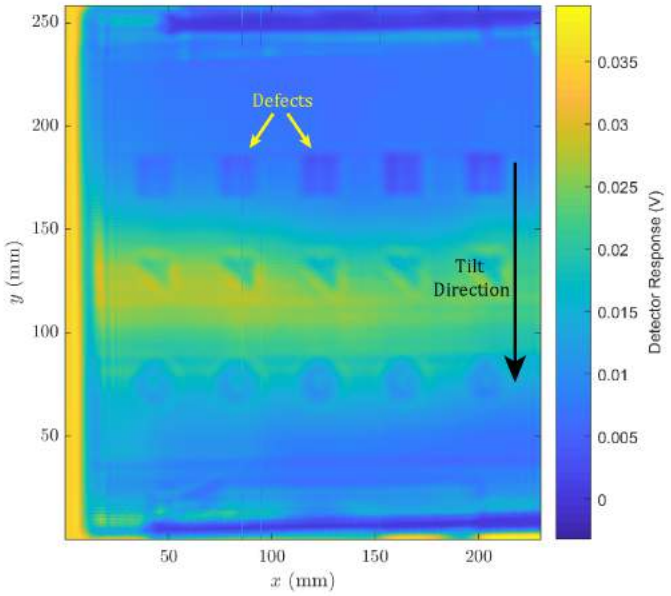

Figure 5.19: Scan of a PLA sample with small defects. The piece is 5 mm thick, the defects are positioned at different depths and are 0.5 mm thick.

A sample with a ramp and steps was produced in PLA. Scanning this part produced the result observed in figure 5.20. According to expectation from previous understanding

of the Fabry-Perot phenomenon, the ramp manifested as a wave pattern. Since it has a variation in height of 6 mm, the expected number of fringes would be 6.0/1.6 = 3.75. On the left side of the ramp, 3 darker regions can be observed horizontally confirming the expectation. On the side of the steps, these manifest as smooth plateaus. Interestingly, not unlike other scans performed, the borders of the steps produce an area where the signal is poorly transmitted.

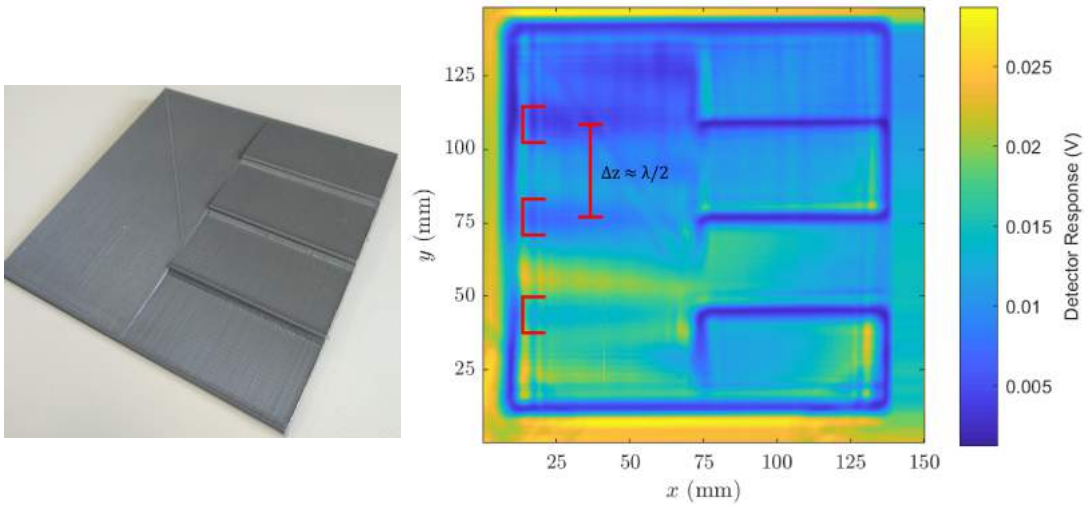

(a) (b)

Figure 5.20: Picture and scan of a PLA sample with a ramp and steps. The ramp is 10 mm thick on the wider side and 4 mm on the thinner. Each step is 2 mm tall. The markers on image (b) indicate areas that respond similarly to the Fabry-Perot effect, indicating a difference in thickness of half the wavelength.

5.5 Analysis of Metallic Wires

Composite materials often consist of a matrix of dielectric material reinforced by strands of a different material. Commonly, the reinforcing material is metallic or carbon fibre based, which, due to its electric conductivity, makes it opaque to terahertz. For some of the composite materials, the strength is dependent on the orientation of the reinforcement. As such, imaging these strands can be of high interest either to analyse the orientation or to search for defects.

To test the system's response to metallic wires, a set of thin enamelled copper wires with diameters between 35 and 500 µm, were laid on an acrylic sheet and a set of C-scans were performed with the sample at different heights while maintaining the detector's height D constant, similarly to what was done previously. The resulting image can be observed in figure 5.21. All wires show a clear contrast in the image, however, similarly to what was observed in figure 5.14, different heights accentuate different effects of the interaction between the radiation and the wires. At 0.05 mm the wires appear as a darker

shadow, while in at 0.15 mm, the diffraction at the edges is more prominent. Despite looking qualitatively different, the exact relations of the dimensions between wires are not obvious.

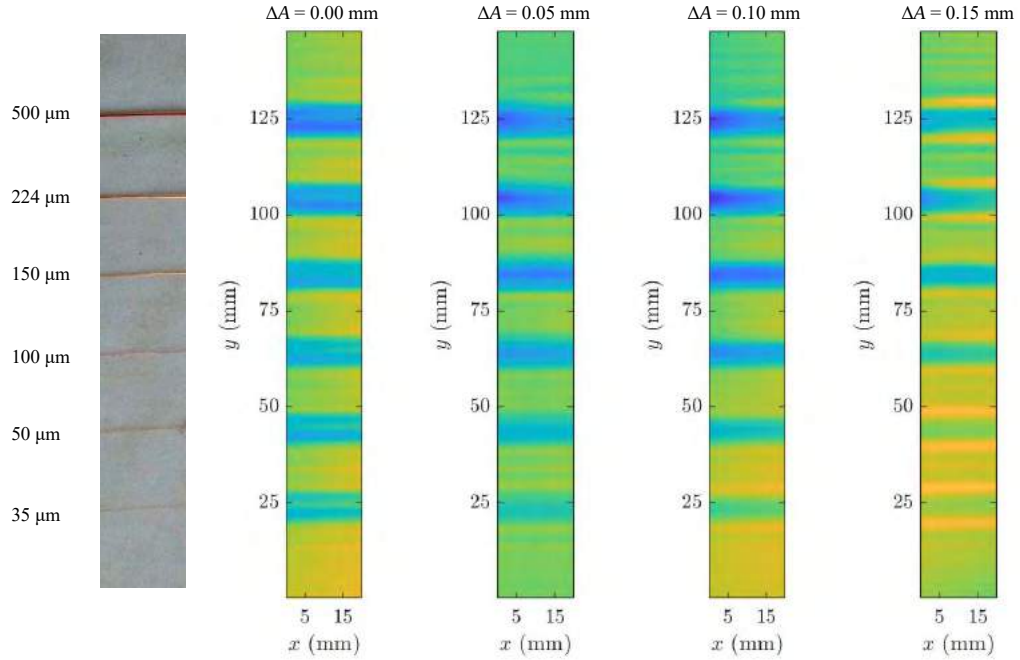

Figure 5.21: Four 20 mm by 150 mm C-scans taken at different heights of a sample consisting of six enamelled copper wires laid on a 7.8 mm thick acrylic sheet. The wires had the diameters of 35, 50, 100, 150, 224 and 500 µm, respectively, from the bottom to the top of the images.

To ensure the wires would be detectable if contained inside the material, as opposed to on top of it, a sample was scanned where two nickel titanium (NiTi) wires were encased in the polymer. The part was composed of PLA and was produced through fused filament fabrication (FFF). Figure 5.22 shows the produced image, where the wires are visible with a contrast similar to previous tests.

Despite being able to detect a 35 µm wire, it is important to note that the resolution of the system is considerably coarser, since the shadow projected by this wire is not representative of its actual size.

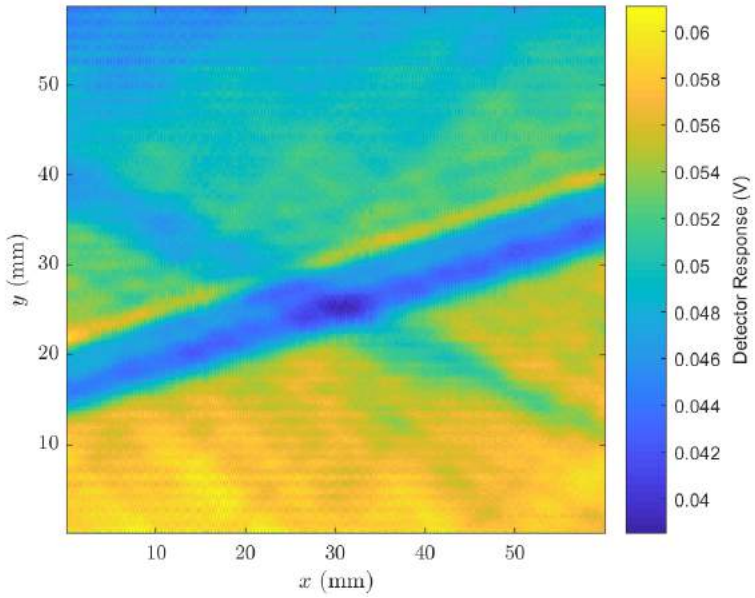

Figure 5.22: Results of a C-scan of a PLA sample containing two crossing NiTi wires, one 150 µm and the other 500 µm thick. A gradient is also visible along the y axis, which was caused by a slight tilt in the sample, similarly to what was described in figure 5.10.

5.6 Comparison with Other Methods

Throughout this work, CW THz imaging has proven to be a reliable method at imaging various types of features. To understand its position in the NDT context, it is important to compare it with other, already established, non-contact imaging techniques.

For this purpose, a sample was produced that included three different features: a delamination/void, a metallic wire and a water infiltration (figure 5.23). The part was constituted of PLA, produced by FFF and was 5 mm thick. Both the void and infiltration are 20×20 mm squares 0.5 mm deep. The wire is 35 µm in diameter. All the features are centred at 1.5 mm from one of the surfaces, as such, these are closer to one of the surfaces of the PLA plate than the other, which is relevant for some techniques.

Apart from CW THz, the tested methods were *Active Transient Thermography*, *Air-Coupled Ultrasounds* and *Digital X-rays*.

5.6.1 Active Transient Thermography

Active thermography is a technique where the part is heated with an external heat source, such as a lamp, and a thermal image is recorded. The recording can happen both during, and after the part is heated. This method highlights parts of the imaged object where the thermal conductivity, thermal heat capacity or geometric shape are different. In a situation where the heating element is placed on the opposite side of the imaged surface, the technique is called *active transient thermography*.

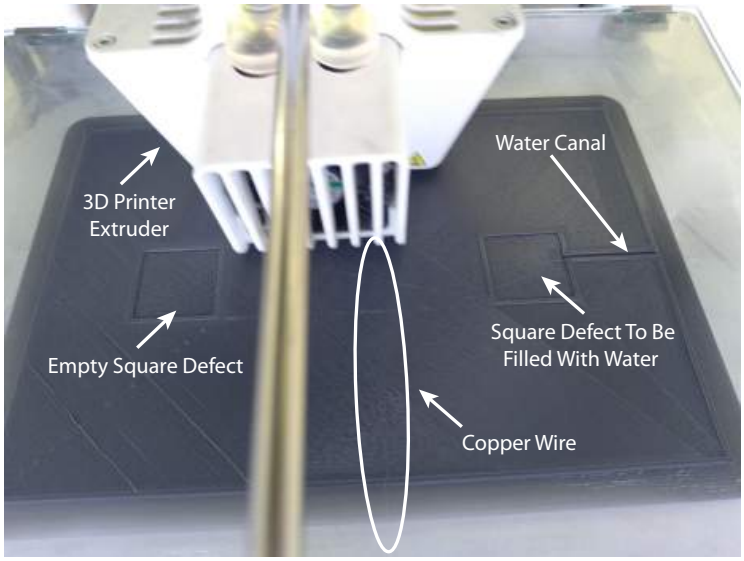

Figure 5.23: Picture taken during the 3D printing of the test piece used to compare the different techniques.

In the performed experiment, the sample was set vertically and heated by four 175 W halogen lamps, 50 cm away, during 20 seconds. As it cooled, the surface's temperature was captured by a Fluke Ti400 infrared camera at a frame rate of 9 Hz. The camera has a temperature measurement range of −20° C to 1200° C. The measurements are performed with a Noise Equivalent Temperature Difference (NETD) of 50 mK, in the spectrum 7.5 to 14.0 µm, an accuracy of ±2° C and spatial resolution (iFOV) of 2.62 mRad. Because the features in the part were closer to one of the surfaces, an image was taken at each side. The resulting images shown in figure 5.24 are the frames from each video where the contrast is highest. The empty defect can be seen in both images, while the one with infiltrated water can has very poor contrast when farther from the surface. This defect manifests as wide area because the water infiltrated in the PLA itself. The copper wire is invisible in both cases. The entire process of heating and recording took about two minutes for each side. This time can vary depending on the material, geometry and heating element, but generally will remain in the order of a few minutes.

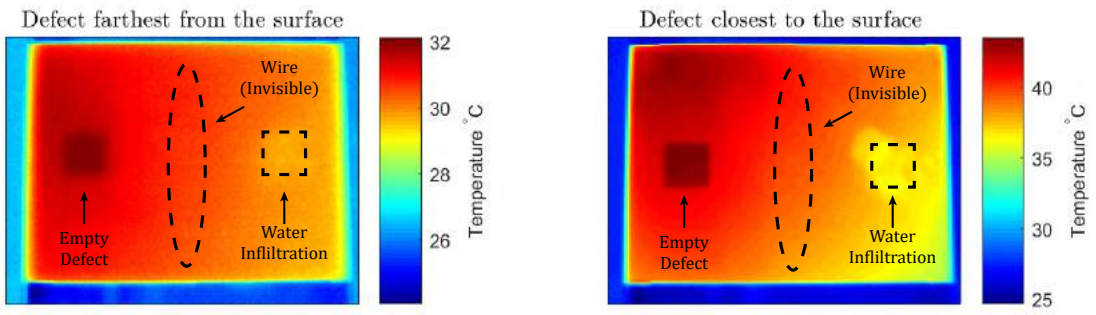

Figure 5.24: Two thermal images taken from either side of the sample. Both were the frames with higher contrast picked from the thermal video.

5.6.2 Air-Coupled Ultrasounds

Ultrasound imaging is a technique that employs sonic waves with frequencies beyond the human hearing range, to produce an image. The image can be constructed from either the time delay or amplitude loss of the signal at each point. Traditionally, this method requires direct contact between the probes and the imaged subject. However, in some situations, direct contact may not be practical or even possible.

Air-Coupled ultrasonic imaging solves this issue by using the air as a coupling medium, effectively eliminating the need for direct contact at the expense of having a worse SNR.

The ultra-sonic images acquired resorted to a non-contact, transmission setup using the scanner described in Section 4. Both the excitation and sensitive piezoelectric probes with 11 mm diameter were set at 40 mm from each side of the sample. The air-coupled equipment was a DIO 1000 LF Flaw Detector from Starmans^{TM} operating in pulses of 200 kHz wave packets and measuring both the attenuation and time of flight. Figure 5.25 shows the resultant images. Both were obtained from the same scan but one shows attenuation while the other shows the delay of the pulse. Both square defects are visible, but the defect without the water shows a higher contrast. The bright spots seen in the attenuation scan on the defect filled with water were caused by air bubbles, which can also be seen in the X-Ray image. The metallic wire was undetected by this technique. The scan presented was taken at steps of 0.25 mm for an area of 130×180 mm which took about 34 minutes for both sets of data, as these are acquired simultaneously. Since the scans were preformed in a raster-pattern, the time scales linearly with the scanned area and inversely with the step size. However, it is important to note that in the performed scans, the limiting factor was the mechanical speed of the scanner. With a sturdy and precise scanner, these could have been performed considerably faster. Nonetheless, the nature of US imaging imposes a speed limitation bound to the speed of sound itself as it is discussed in [34].

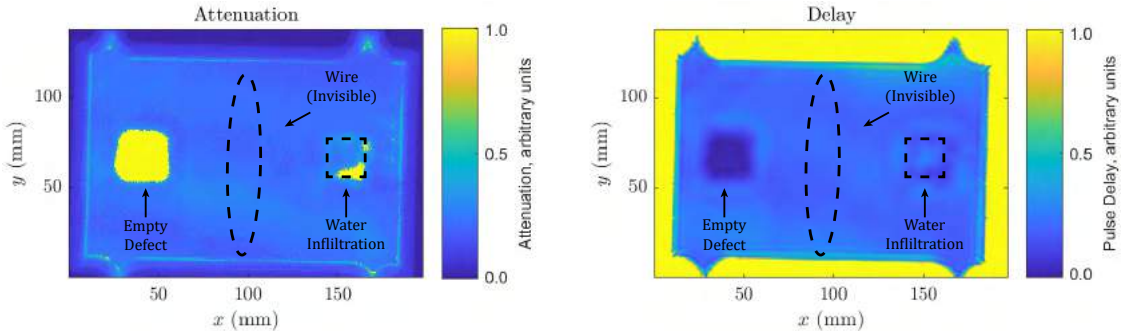

Figure 5.25: Images acquired from the ultra-sound C-scan. The one on the left shows attenuation and the one on the right shows the delay of the pulse.

5.6.3 Digital X-rays

X-ray imaging is a process that consists in irradiating the subject with high energy photons and measuring the quantity that is able to permeate through. Traditionally, it was used for medical applications and the image was produced by a *photographic plate* that reacted to high energy radiation. These days, *digital x-rays* use electronic sensor arrays to acquire the images, and the technique is used in applications beyond the medical sector. This method is usually regarded for its high versatility and resolution. Nonetheless, as it is verified further on, there are limitations. Additionally, the use of ionising radiation raises the need for special care for human safety in these systems.

The X-ray imaging was performed using a *Kodak 2100 X-ray System*, which has a 60 kV 7 mA bulb and a 22×30 mm detector with a spatial resolution of 30 micron and a 32bit greyscale. Figure 5.26 shows the produced images. Both the empty defect and the wire are clearly visible. However, in the defect filled with water only the bubbles and the canal are visible. This occurs because by volume, the water attenuation of x-rays is similar to that of PLA. As it is characteristic of X-ray imaging, these images were acquired effectively in an instant.

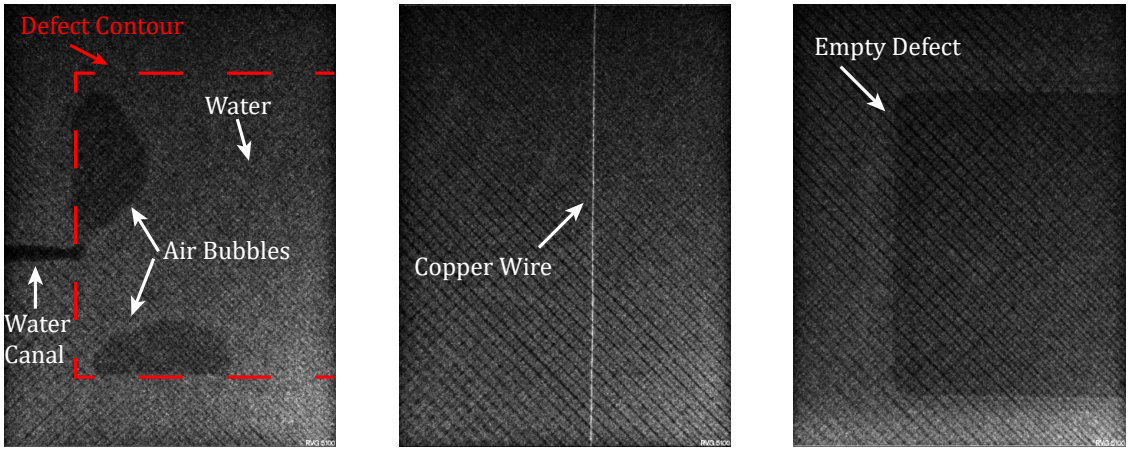

Figure 5.26: X-ray images of the three points of interest of the sample. From left to right: the defect filled with water with two air bubbles, the 35 µm enamelled copper wire and the empty defect. The image colours is reversed in the sense that the brightest areas correspond to where the radiation was less transmitted. On the water filled defect image, a red dashed line delimits the defect.

5.6.4 Continuous Wave Transmission Terahertz

Finally, figure 5.27 shows the results of the THz scan. Because of the effect seen in figure 5.14, the scan was performed at different heights. At any height, all three features are visible even if with differing contrasts. Because of the way water absorbs THz, the defect filled with water shows the highest contrast. Around the bottom left corner of this square, a darker area can also be seen which was caused by water that soaked into the

PLA itself. This infiltration seems smaller that the one seen in the thermography images, because that test was performed later, which allowed the water to penetrate further. The canal used to fill it is also visible in these scans. The empty square defect is clearly visible as its edges are evidenced by diffraction effects. Finally, the 35 µm copper wire, despite being thinner than the employed wavelength, is visible running through the middle of the sample. The THz scans were performed using the same scanner as the non-contact ultrasound scans. As such, a scan with the same dimensions (130×180 mm) and step size (0.25 mm) will take the same time (34 min). However, if as it is proposed in this article, multiple scans are taken, the spent time will get multiplied. Similarly to the US scans, the time scales linearly with the scanned area and inversely with the step size. Still akin to US, the limitation on the speed of the scans performed was the mechanical speed itself, which could be greatly improved with a faster scanner. Unlike the US, CW THz imaging does not abide to the limitation of the speed of sound. As such, with a specialised scanner, this method could theoretically acquire images at up to one million pixels per second, limited by the detectors response time of 1 µm.

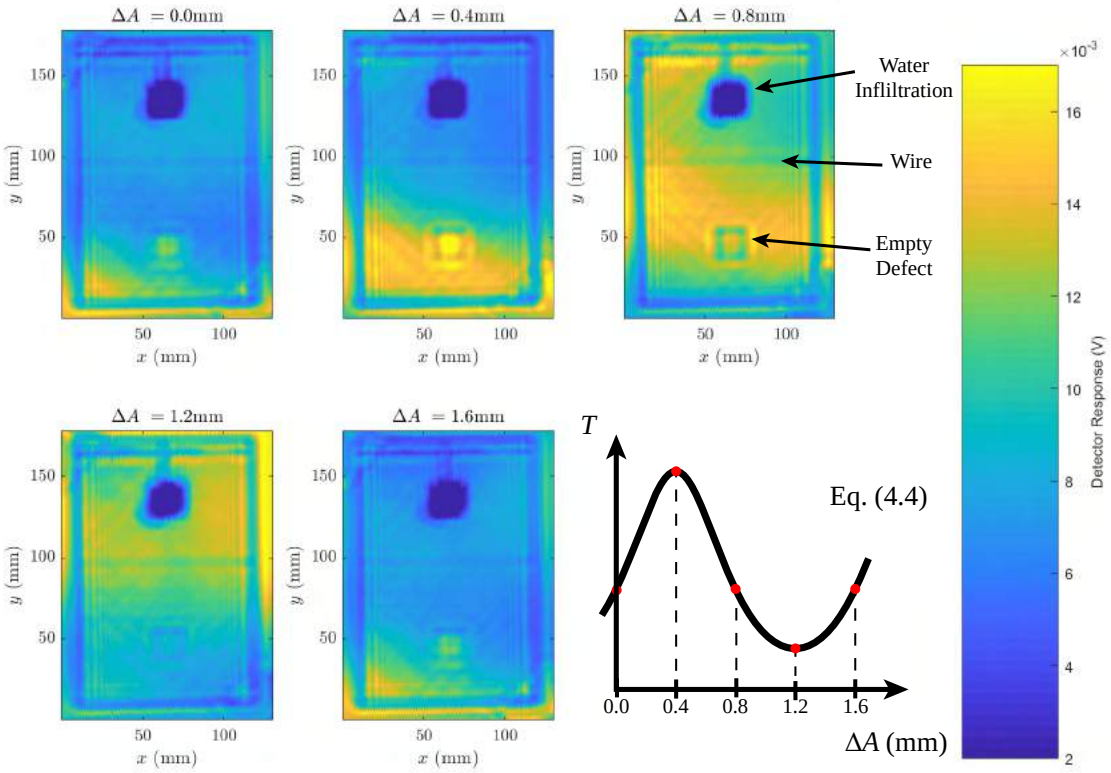

Figure 5.27: Terahertz scans of the test piece done at different heights (similarly to what was done in figure 5.14). The top square is the one filled with water. On the bottom right, a graph shows the expected variation of the response when varying A, according to equation (5.4).

Gathering the information from these tests, Table 5.1 was created to summarise the results.

Table 5.1: Value proposition of the different NDT methods to for the analysis of the same sample.

	Empty Defect	Water Infiltration	Metallic Wire	Typical Time	Health Safety
CW Terahertz Imaging	✓	✓✓✓	✓	34 × 5 minutes	✓
Air-Coupled Transmission US	✓	✓	×	34 minutes	✓
Active Transient Thermography	✓	✓*	×	2 × 2 minutes	✓
Digital X-Ray Imaging	✓✓✓	×	✓✓✓	Instantaneous	×

* Only when close to the surface

5.7 Reflection Setup

This work focuses mainly on a transmission setup for terahertz imaging where a emitter and detector are placed on either side of the subject. However, for some applications it is necessary to operate with both the source and detector on the same side. This restriction can arise from a material that has a layer that reflects the radiation blocking it from reaching the other face, or simply for accessibility reasons, where it may no the possible to have a detector on the opposite side. Hence there was an interest to test the capabilities of the available equipment in a reflection setup.

The system was setup with the source and detector at a 45° angle from the sample, as shown in figure 5.28. The goal was for the wave to reflect of the sample and hit the detector. Nevertheless, all the scans were performed with the sample at different heights to ensure the best position was covered.

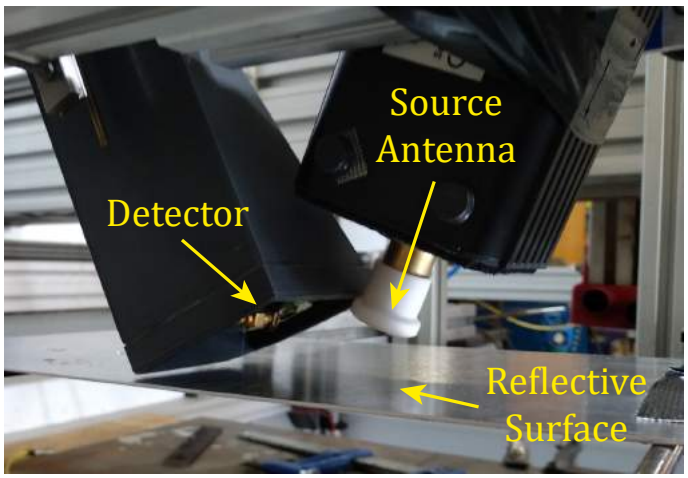

Figure 5.28: Picture of the reflection setup.

The first scanned object was an acrylic plate. The scan consists in 100 mm lines that start in the middle of the surface and move out of the plate. 50 of these lines were scanned raising the height 0.1 mm each time, so that 5 mm were covered. Figure 5.29 shows the resulting data, and figure 5.30 shows a single line scan at the height of 2.5 mm. While there is a region where the signal loss is stronger, evidencing the reflection in the plate, the overall SNR is low and there is a lack of contrast in the edge. It is important to note that for geometric reasons, this disposition forces the total path travelled by the radiation to be considerably longer than in a transmission setup. Consequently, the dispersion of the beam is more evident, which is likely the cause for the lack of contrast.

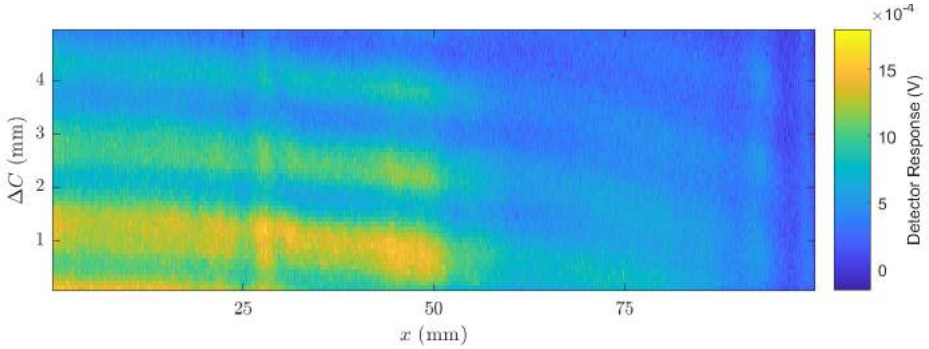

Figure 5.29: Scans of the edge of an acrylic plate in a reflection setup varying the distance of the plate at each line. The board occupies the left side of the scan until 50 mm.

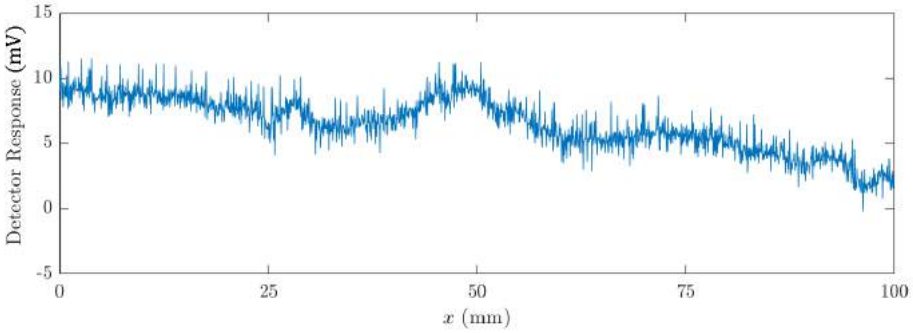

Figure 5.30: Single line at $\Delta C = 2.5$ mm from figure 5.29.

After testing some other samples, it was found that the best results were produced by copper wires laid on an acrylic plate, similarly to what was done in figure 5.21. The results are shown in figures 5.31 and 5.32. Here, the wires can be seen as brighter vertical streaks representing points were the metal reflected a higher portion of the radiation. Nevertheless, the contrast and SNR remain worse than what was possible with transmission imaging.

We can then conclude that while possible, reflection imaging is not viable using this type of equipment and setup. Hypothetically, using a set of lenses could be useful to converge the beam, reducing the resolution loss caused by the bigger optical path.

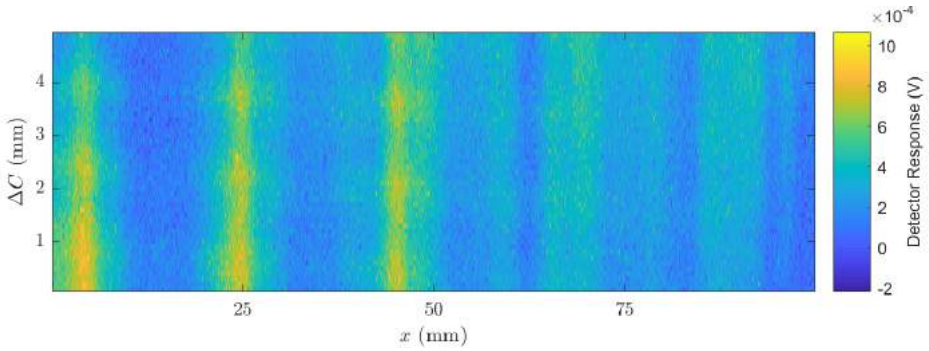

Figure 5.31: Scans of an acrylic plate in a reflection setup varying the distance of the plate at each line. The wires are spaced 20 mm apart, and have the diameters of 500, 224, 150, 100 and 50 µm, from left to right respectively.

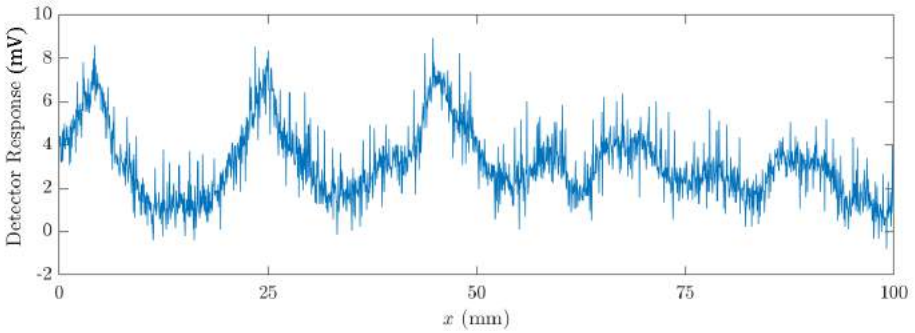

Figure 5.32: Single line at $\Delta C = 2.5$ mm from figure 5.31.

5.8 Other Applications

To search for applications other than NDT, the system was used to scan a variety of other objects. Figure 5.33 shows a scan done to a green *Platanus* leaf. The different amounts of moisture in the various areas of the leaf, absorb the radiation accordingly thus producing the image. This shows potential as a technique to image the water distribution in plants or other organic forms. Because of the sensitivity of terahertz radiation to water, measuring the water content in biological samples is a widely researched application. It has been studied as early as 1995 with the work of Hu *et al.* [35] and more recently quantitative measurements have been performed [36], [37].

In recent years, terahertz imaging has seen a variety of applications in security. Some airports now employ walk-in terahertz scanners as a replacement of a "manual search". The system presented in this work was tested with a magazine containing a pair of steel scissors (figure 5.34). As expected, the scissors are clearly visible through the 106 pages, but a stripped pattern can also be observed which is caused by the curvature of the cover. As it is non-ionizing, terahertz has potential applications in the security sector. For this application, it is important for the equipment to be cost effective, easy to operate and have a low footprint. As such, CW THz imaging proves as an adequate candidate as it was studied in further detailed in several articles [11], [38].

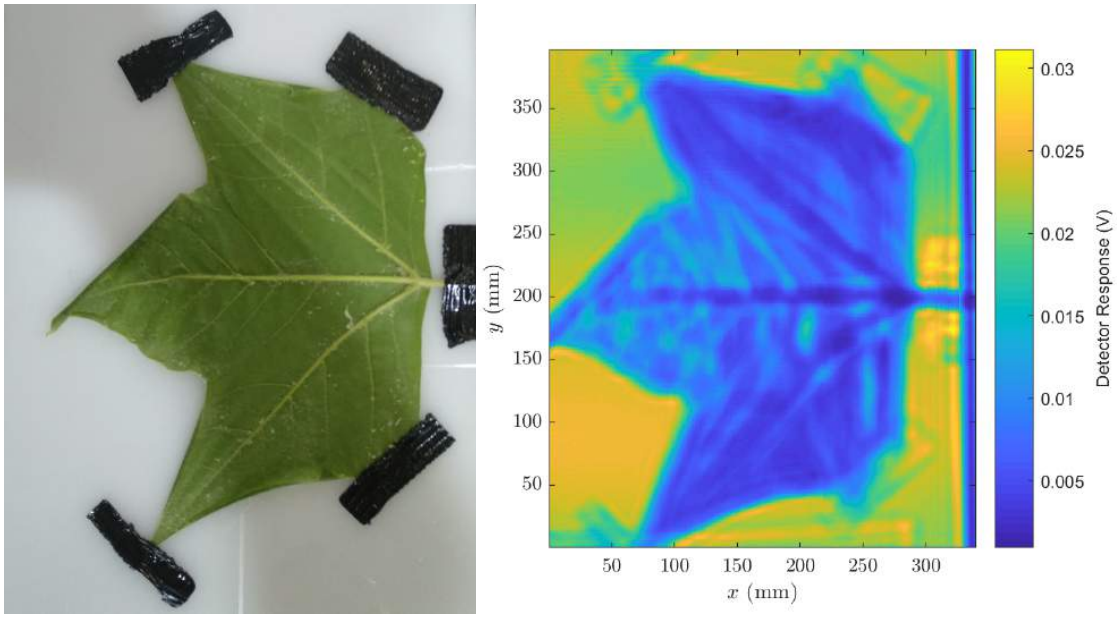

Figure 5.33: Picture and scan of a *Platanus* leaf.

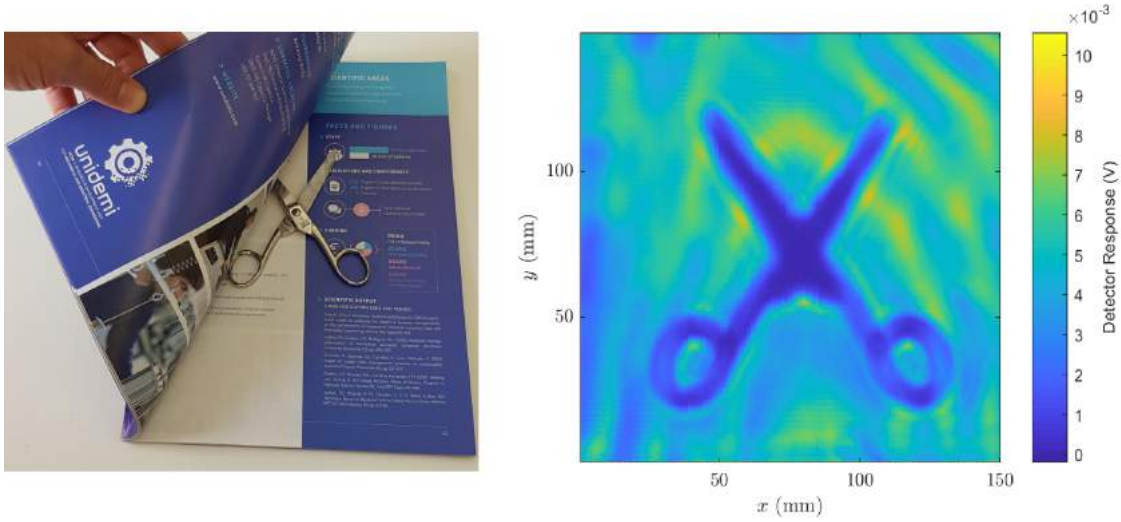

Figure 5.34: Picture and scan of a magazine with a pair of steel scissors inside. The magazine is 106 pages long, which corresponds to a thickness of about 4 mm.

A 20 € banknote was scanned between two acrylic plates. Figure 5.35 shows the resulting image compared to the picture of the banknote. Both the security stripe and the metallic strip are detected. This opens the possibility of CW THz to be used to detect counterfeits. In a practical application the scanning could be done rapidly as only one line needs to be scanned.

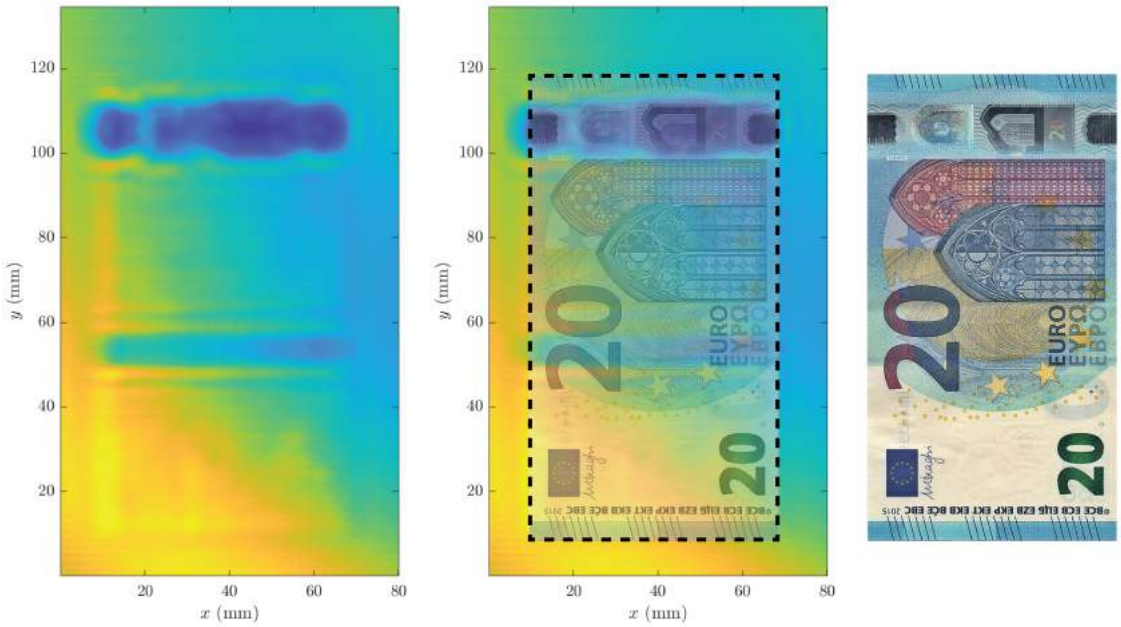

Figure 5.35: Picture and scan of a 20 € banknote. The security stripe and the metallic strip are visible. Additionally, a gradient caused by a slight tilt of the sample is also visible.

5.9 Numerical Simulations

The *Finite Element Method*, is a numerical method widely used in engineering as a means to simulate and solve problems. To achieve a solution, the system is subdivided into smaller and simpler fractions names *finite elements*. The differential equations describing the phenomenon are solved for each element individually and the solutions are assembled to model the entire system. Finally, to approximate the solution, *variational methods* are employed by interpolation, as to minimise the associated error function [39].

To get a better insight on the observed interactions of terahertz with different materials and geometries, a set of simulations were performed using the *Ansys HFSS*^{TM} software. figure 5.36 shows the geometric model and mesh used in the simulations. The source is a metal circle with a diameter of 16 mm and the detector is a 10×10 mm metal square, which corresponds to the area of the metallic frame around the detector's sensitive area. The properties of all the used materials can be found in appendix D. Both the detector and source need to be simulated in order to account for reflections, and consequently, the Fabry-Perot effect. The mesh was composed of 500 000 tetrahedral elements. The wave port was used with a Finite Element-Boundary Integral (FE-BI) hybrid region. It is important to note that while the colour-scale is the same between two images in the same figure, it is not necessarily the same between images on separated figures. The source was simulated to emit radiation at 0.094 THz.

The following images show a vertical middle cut of the simulated area, where the

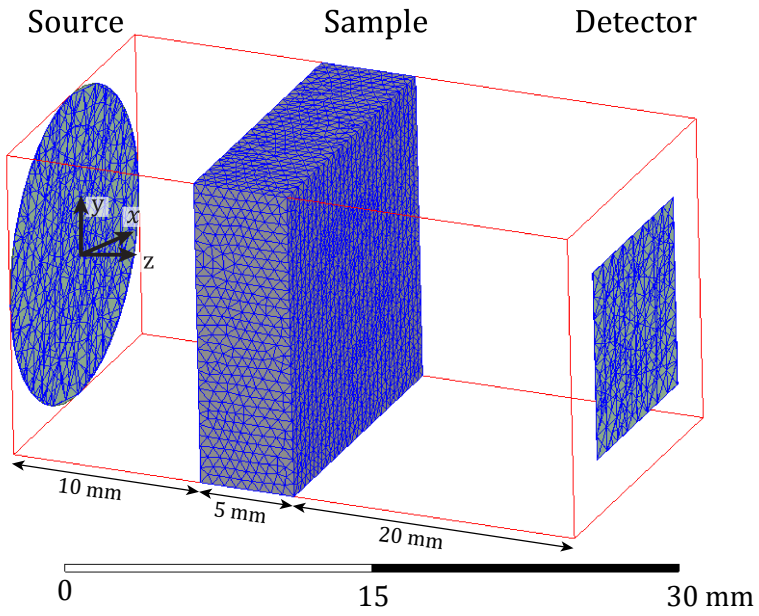

Figure 5.36: Geometric model, main components and mesh used in the numerical simulations.

colour-scale represents the *absolute amplitude* of the simulated electric field at phase 0°. Animated GIFs showing the simulation results from phase 0° to 360°, can be found **here**. The properties of each simulated material can be found in appendix D.

Figure 5.37 shows the comparison between the results in a simulation with, and without the PLA sample, without any defects. The wavelength is shorter inside the polymer (≈ 2.6 mm) than on air (≈ 3.2 mm) due to its higher refractive index. This positioning of the sample also produces a lower electric field next to the detector. This is caused by a combination of the attenuation and dispersion, and the Fabry-Perot effect.

In figure 5.38, a comparison between a sample with and without a 100 µm wire running through it is shown. Similarly to the experimental results, the amplitude close to the detector is lower in the presence of the wire. The simulation also provided some insight on how the wire deforms the radiation beam, which would otherwise be difficult to observe since the presence of the detector influences the field itself.

Figure 5.39 shows the results of a sample with a defect filled with water. As expected, the water absorbs most of the radiation. These results are validated further by figure 5.27.

Figure 5.40, presents the results for a defect filled with air. The intensity of the electric field next to the detector was higher when compared to the case without the defect. This result is similar to what was observed in figure 5.14 at the heights 0.2, 0.4 and 1.8 mm.

On the scans performed in figure 5.14, the borders of the defects produced a contour of low intensity. To study this effect, the simulation shown in figure 5.41 was performed. The results, in agreement with the experiment, showed that when the beam goes over the interface, a shadow is produced in what appears to be a diffraction effect.

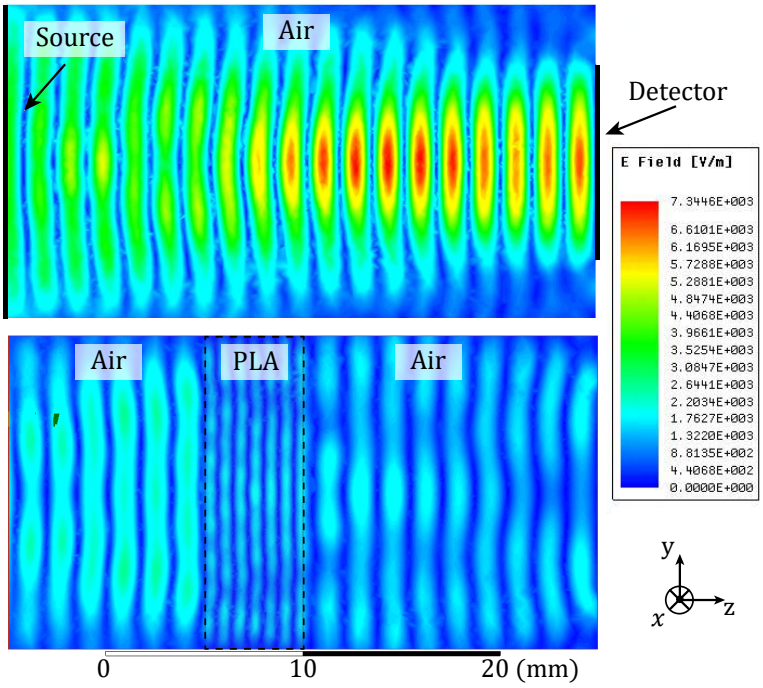

Figure 5.37: Resulting electric field of the simulation without and with a 5 mm thick PLA sample. The wavelength can be observed to contract inside the polymer. Note that because the image shows the absolute amplitude of the electric field, one wavelength corresponds to the distance between every other peak.

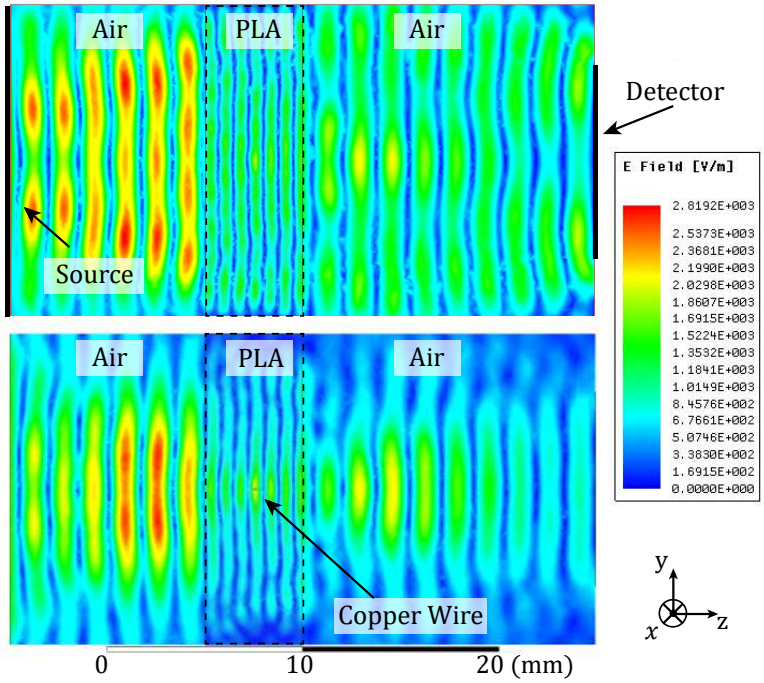

Figure 5.38: Resulting electric field of the simulation of a 5 mm thick PLA sample without and with a 100 µm copper wire running in the middle.

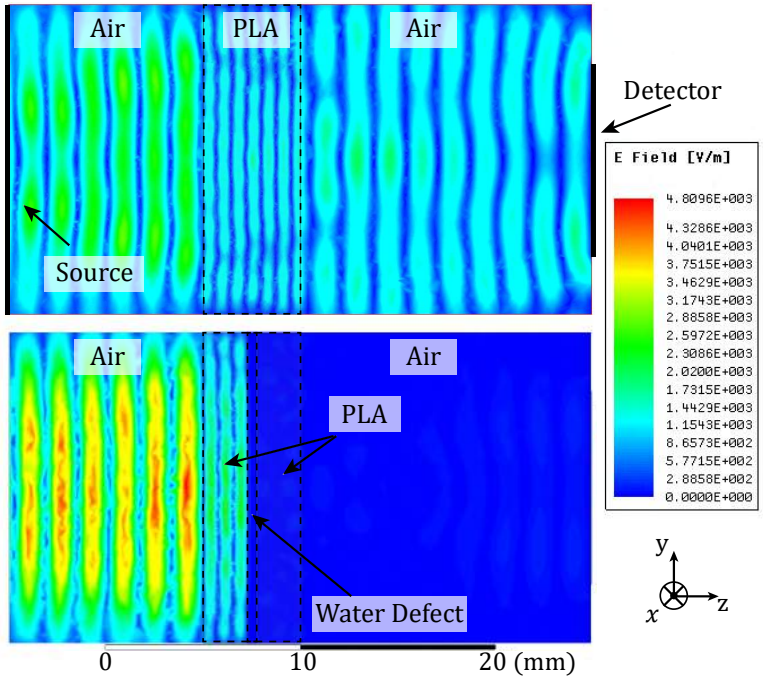

Figure 5.39: Resulting electric field of the simulation of a 5 mm thick PLA sample without and with a 0.4 mm thick defect of water in the middle.

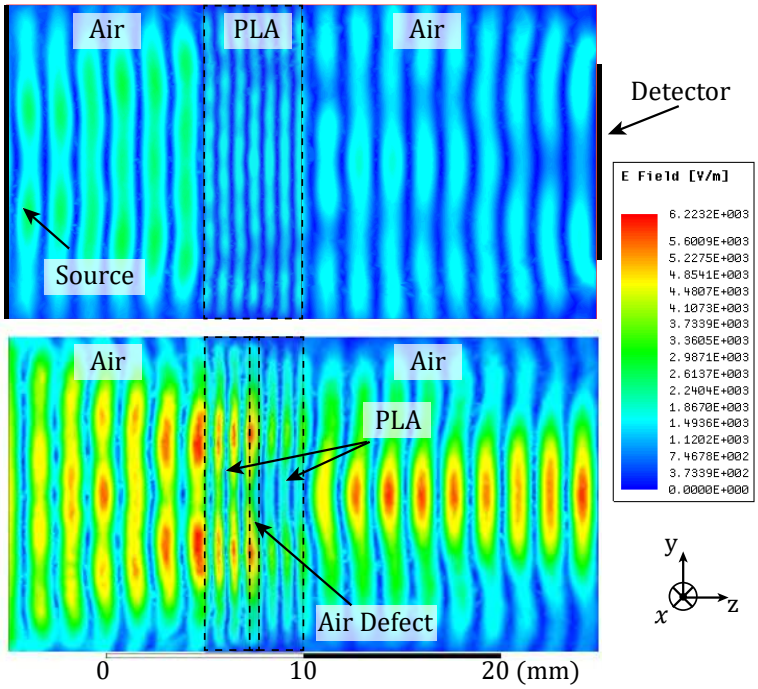

Figure 5.40: Resulting electric field of the simulation of a 5 mm thick PLA sample without and with a 0.5 mm thick defect of air in the middle.

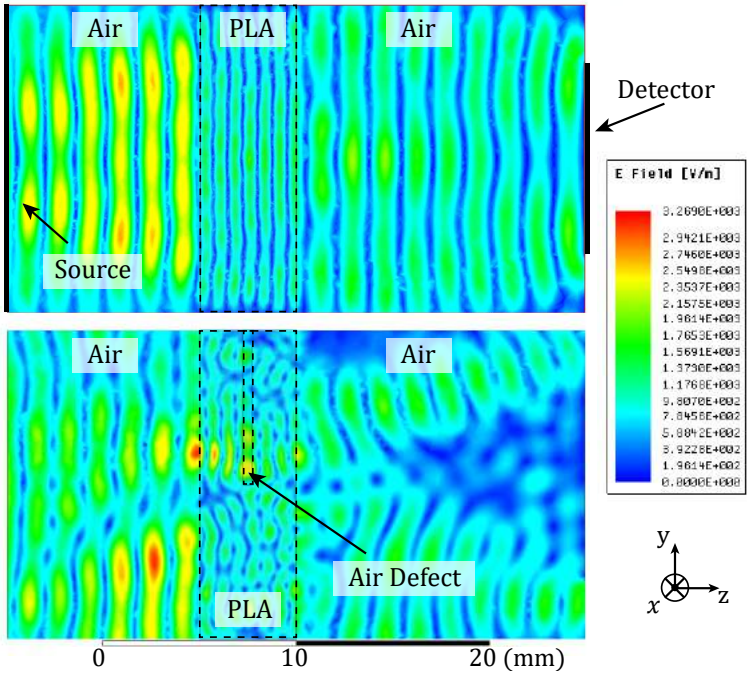

Figure 5.41: Resulting electric field of the simulation of a 5 mm thick PLA sample without and with a 0.5 mm thick layer of air in the middle, spanning through half the width of the sample.

For electromagnetic wave simulations, the size of the elements are limited by the wavelength of the radiation. This makes terahertz simulations highly computation demanding, which proved to be a limiting factor. In a few years, the rapid advances in consumer grade computing technology will allow for more complex and useful simulations.

Chapter 6

Conclusions

In the work described in this thesis, developments were made for different areas of CW THz imaging, building the foundations for further investigation of this technique. From a technological standpoint:

- A prototype was built that can be mounted on a CNC table to perform scans, which proved to be adequate and reliable for the experimentation.
- The software to accompany the prototype was also built, consisting of a LabView program to control the scanner and acquire the data, and a MATLAB script to process the image.
- A characterisation of the source and detector was made, from which the beam was observed to have a Gaussian shape, and an exponential equation was obtained that describes the intensity decay.
- An issue with motor acceleration was identified and a solution was employed in the MATLAB script, where every other line is shifted according to the scanning speed, resolution and acceleration.
- Different forms of deconvolution were tested namely blind deconvolution, Richardson-Lucy deconvolution and Wiener filtering. Wiener filtering produced the best results, allowing for thin vertices to be restored.

In terms of experimental developments:

- Several samples with different features were 3D modelled and printed, such as voids with different shapes and sizes, ramps, steps, encased copper wires and water infiltrations.

- The system was tested with polymeric samples, where it was found to be effective at detecting delaminations and extremely effective at detecting water infiltrations.
- Copper wires with different diameters were scanned, both isolated and contained in a polymeric sample, which the system excelled at detecting down to diameters of 35 µm.
- A sample was modelled and produced specifically to be compared with other non-contact NDT methods, which was composed of a polymeric sample with a square void, a 35 µm copper wire, and a water infiltration.
- This sample was imaged by *Active Transient Thermography*, *Air-Coupled Ultrasounds*, *Digital X-rays* and CW THz, from which a value proposition table was produced, showing that CW THz provides complementary information of high interest to NDT.
- A method for enhancing the resolution using diaphragms was tested, which revealed that an aperture of 1.6 mm produces images of higher resolution at the expense of a worse SNR.
- A reflection setup was tested showing as a proof of concept, where it was demonstrated that the signal intensity and SNR are highly compromised.
- Other objects were scanned, such as a tree leaf, scissors in a magazine and a banknote, where various features were successfully imaged opening the possibility of applications of this technique beyond NDT.

The progress in mathematical comprehension of the Fabry-Perot effect in CW THz imaging:

- The Fabry-Perot effect was identified as the source of background gradients on the scans. It was then characterised experimentally with high detail and accuracy.
- Iterative attempts to mathematically model the effect showed that for an accurate model, a matrix method needs to be used and energy losses need to be considered.
- A MATLAB code was created using the model that accurately agrees with experiment. Such a model is not yet been found in the bibliography.
- Through the comprehension of this effect a new measurement application was proposed and demonstrated, where the gradients caused are used to measure thickness variations and tilt.
- The influence this effect had on imaging was tested and a method of multiple scans was proposed, where a full characterisation of the observed features is guaranteed.

A numerical simulation approach was also developed as a means to analyse the involved phenomena, from which:

- The system was modelled and a mesh was built in Ansys Electromagnetics HFFS.
- A simulation of a copper wire contained in a polymeric sample agreed with experimentation, where a thin wire caused a severe attenuation of the transmitted intensity.
- A simulation of an empty defect revealed an effect experimentally observed, where the centre of the defect shows a bright spot.
- A simulation of the border of an empty defect revealed a diffraction effect that allowed for the comprehension of shadows in material discontinuities.

Concluding, the work shown in this thesis provided solid foundations and *know-how* in the technological, experimental, mathematical and numeric aspects of continuous-wave terahertz imaging, some of which innovative in the field. Further works can now be built upon what is here presented.

Bibliography

[1] D. M. Mittleman, M. Gupta, R. Neelamani, R. G. Baraniuk, J. V. Rudd, and M. Koch, "Recent advances in terahertz imaging," *Applied Physics B: Lasers and Optics*, vol. 68, no. 6, pp. 1085–1094, 1999, ISSN: 09462171. DOI: 10.1007/s003400050750.

[2] C. Sirtori, "Applied physics: Bridge for the terahertz gap," *Nature*, vol. 417, no. 6885, pp. 132–133, 2002. DOI: 10.1038/417132b.

[3] D. H. Auston, A. M. Glass, and P. Lefur, "Tunable far-infrared generation by difference frequency mixing of dye lasers in reduced (black) lithium niobate," *Applied Physics Letters*, vol. 23, no. 1, pp. 47–48, 1973. DOI: 10.1063/1.1654733.

[4] K. H. Yang, J. R. Morris, P. L. Richards, and Y. R. Shen, "Phase-matched far-infrared generation by optical mixing of dye laser beams," *Applied Physics Letters*, vol. 23, no. 12, pp. 669–671, 1973. DOI: 10.1063/1.1654785.

[5] W. Lam Chan, "Imaging with terahertz radiation," *Reports on Progress in Physics*, vol. 70, no. 8, p. 1325, 2007. DOI: 10.1088/0034-4885/70/8/R02.

[6] M. Tonouchi, "Cutting-edge terahertz technology," vol. 1, no. 2, pp. 97–105, 2007. DOI: 10.1038/nphoton.2007.3.

[7] N. Yaekashiwa, H. Yoshida, S. Otsuki, S. Hayashi, and K. Kawase, "Verification of non-thermal effects of 0.3-0.6 THz-waves on human cultured cells," *Photonics*, vol. 6, no. 1, p. 33, 2019. DOI: 10.3390/PHOTONICS6010033.

[8] C. Stoik, M. Bohn, and J. Blackshire, "Nondestructive evaluation of aircraft composites using reflective terahertz time domain spectroscopy," *NDT and E International*, vol. 43, no. 2, pp. 106–115, 2010. DOI: 10.1016/j.ndteint.2009.09.005.

[9] D. Zimdars, J. S. White, G. Stuk, A. Chernovsky, G. Fichter, and S. Williamson, "Large area terahertz imaging and non-destructive evaluation applications," *Insight: Non-Destructive Testing and Condition Monitoring*, vol. 48, no. 9, pp. 537–539, 2006, ISSN: 13542575. DOI: 10.1784/insi.2006.48.9.537.

[10] J. Dong, B. Kim, A. Locquet, P. McKeon, N. Declercq, and D. S. Citrin, "Nondestructive evaluation of forced delamination in glass fiber-reinforced composites by terahertz and ultrasonic waves," *Composites Part B: Engineering*, vol. 79, pp. 667–675, 2015. DOI: 10.1016/j.compositesb.2015.05.028.

[11] N. Karpowicz, H. Zhong, J. Xu, K.-I. Lin, J.-S. Hwang, and X.-C. Zhang, "Comparison between pulsed terahertz time-domain imaging and continuous wave terahertz imaging," *Semiconductor Science and Technology*, vol. 20, no. 7, S293, 2005. DOI: 10.1088/0268-1242/20/7/021.

[12] Y. H. Tao, A. J. Fitzgerald, and V. P. Wallace, "Non-Contact, Non-Destructive Testing in Various Industrial Sectors with Terahertz Technology," *Sensors*, vol. 20, no. 3, p. 712, 2020. DOI: 10.3390/s20030712.

[13] K. J. Siebert, H. Quast, R. Leonhardt, *et al.*, "Continuous-wave all-optoelectronic terahertz imaging," *Applied Physics Letters*, vol. 80, no. 16, pp. 3003–3005, 2002. DOI: 10.1063/1.1469679.

[14] H. Zhong, N. Karpowicz, J. Xu, *et al.*, "Inspection of space shuttle insulation foam defects using a 0.2 THz Gunn diode oscillator," in *Conference Digest of the 2004 Joint 29th International Conference on Infrared and Millimeter Waves and 12th International Conference on Terahertz Electronics*, 2004, pp. 753–754, ISBN: 0780384903. DOI: 10.1109/icimw.2004.1422311.

[15] H. Zhang, S. Sfarra, K. Saluja, *et al.*, "Non-destructive Investigation of Paintings on Canvas by Continuous Wave Terahertz Imaging and Flash Thermography," *Journal of Nondestructive Evaluation*, vol. 36, p. 34, 2017. DOI: 10.1007/s10921-017-0414-8.

[16] S. Takahashi, T. Hamano, K. Nakajima, T. Tanabe, and Y. Oyama, "Observation of damage in insulated copper cables by THz imaging," *NDT and E International*, vol. 61, pp. 75–79, 2014. DOI: 10.1016/j.ndteint.2013.10.004.

[17] Y. Oyama, L. Zhen, T. Tanabe, and M. Kagaya, "Sub-terahertz imaging of defects in building blocks," *NDT and E International*, vol. 42, no. 1, pp. 28–33, 2009. DOI: 10.1016/j.ndteint.2008.08.002.

[18] T. Tanabe and Y. Oyama, "Terahertz non-destructive monitoring for infrastructure components," in *Asia-Pacific Microwave Conference Proceedings, APMC*, vol. 2018-November, Institute of Electrical and Electronics Engineers Inc., 2019, pp. 1471–1473. DOI: 10.23919/APMC.2018.8617139.

[19] K. Ahi and M. Anwar, "Developing terahertz imaging equation and enhancement of the resolution of terahertz images using deconvolution," in *Terahertz Physics, Devices, and Systems X: Advanced Applications in Industry and Defense*, M. F. Anwar, T. W. Crowe, and T. Manzur, Eds., International Society for Optics and Photonics, vol. 9856, SPIE, 2016, pp. 57 –74. DOI: 10.1117/12.2228680.

[20] D. J. Griffiths, *Introduction to electrodynamics*, 4th ed., 6. Boston, MA: Pearson, 2013, vol. 73, pp. 574–574, Re-published by Cambridge University Press in 2017. DOI: 1108420419.

[21] Y. Lee, *Basic Theories of Terahertz Interaction with Matter*, 1st ed. Boston, MA.: Springer US, 2009, pp. 11–17, ISBN: 978-0-387-09540-0.

[22] W. Hayt and J. Buck, *Engineering Electromagnetics*, 5th ed. Akron, Ohio: McGraw-Hill, 1989, pp. 356–364, ISBN: 0070612234.

[23] E. Hecht, *Optics*, 5th ed. San Francisco, CA: Addison Wesley, 2002, p. 128, ISBN: 9780133977226.

[24] G. Zaccanti and P. Bruscaglioni, "Deviation from the lambert-beer law in the transmittance of a light beam through diffusing media: Experimental results," *Journal of Modern Optics*, vol. 35, no. 2, pp. 229–242, 1988. DOI: 10.1080/09500348814550281.

[25] M. Naftaly, R. Miles, and P. Greenslade, "THz transmission in polymer materials -2014; a data library," in *2007 Joint 32nd International Conference on Infrared and Millimeter Waves and the 15th International Conference on Terahertz Electronics*, IEEE, 2007, pp. 819–820. DOI: 10.1109/ICIMW.2007.4516747.

[26] C. Huygens. Echo Library, 2007, p. 19, ISBN: 3748117124, 9783748117124.

[27] J. Kokkoniemi, P. Rintanen, J. Lehtomäki, and M. Juntti, "Diffraction effects in terahertz band - Measurements and analysis," in *2016 IEEE Global Communications Conference, GLOBECOM 2016 - Proceedings*, Institute of Electrical and Electronics Engineers Inc., 2016. DOI: 10.1109/GLOCOM.2016.7841734.

[28] I. Radiocommunication Bureau, "RECOMMENDATION ITU-R P.526-15 - Propagation by diffraction," Tech. Rep. [Online]. Available: http://www.itu.int/ITU-R/go/patents/en.

[29] A. Osseiran, F. Boccardi, V. Braun, *et al.*, "Scenarios for 5G mobile and wireless communications: The vision of the METIS project," *IEEE Communications Magazine*, vol. 52, no. 5, pp. 26–35, 2014. DOI: 10.1109/MCOM.2014.6815890.

[30] D. A. Fish, J. G. Walker, A. M. Brinicombe, and E. R. Pike, "Blind deconvolution by means of the Richardson–Lucy algorithm," *Journal of the Optical Society of America A*, vol. 12, no. 1, p. 58, 1995. DOI: 10.1364/josaa.12.000058.

[31] E. Y. Lam and J. W. Goodman, "Iterative statistical approach to blind image deconvolution," *Journal of the Optical Society of America A*, vol. 17, no. 7, p. 1177, 2000. DOI: 10.1364/josaa.17.001177.

[32] R. Hardie, "A fast image super-resolution algorithm using an adaptive Wiener filter," *IEEE Transactions on Image Processing*, vol. 16, no. 12, pp. 2953–2964, 2007. DOI: 10.1109/TIP.2007.909416.

[33] H. van de Stadt and J. M. Muller, "Multimirror Fabry–Perot interferometers," *Journal of the Optical Society of America A*, vol. 2, no. 8, p. 1363, 1985. DOI: 10.1364/josaa.2.001363.

[34] D. Dhital and J. R. Lee, "A Fully Non-Contact Ultrasonic Propagation Imaging System for Closed Surface Crack Evaluation," *Experimental Mechanics*, vol. 52, no. 8, pp. 1111–1122, 2012. DOI: 10.1007/s11340-011-9567-z.

[35] B. B. Hu and M. C. Nuss, "Imaging with terahertz waves," *Optics Letters*, vol. 20, no. 16, p. 1716, 1995. DOI: 10.1364/ol.20.001716.

[36] N. V. Chernomyrdin, A. S. Kucheryavenko, G. S. Kolontaeva, *et al.*, "Reflection-mode continuous-wave 0.15 λ -resolution terahertz solid immersion microscopy of soft biological tissues," *Applied Physics Letters*, vol. 113, no. 11, p. 111 102, 2018. DOI: 10.1063/1.5045480.

[37] A. V. Shchepetilnikov, A. M. Zarezin, V. M. Muravev, P. A. Gusikhin, and I. V. Kukushkin, "Quantitative analysis of water content and distribution in plants using terahertz imaging," *Optical Engineering*, vol. 59, no. 06, p. 1, 2020. DOI: 10.1117/1.oe.59.6.061617.

[38] L. Hou, H. Park, and X. C. Zhang, "Terahertz wave imaging system based on glow discharge detector," *IEEE Journal on Selected Topics in Quantum Electronics*, vol. 17, no. 1, pp. 177–182, 2011. DOI: 10.1109/JSTQE.2010.2045640.

[39] D. Logan, *First Course in the Finite Element Method*, Logan, D.L., Ed. Platteville: Thomson, 2007, pp. 1–2, ISBN: 9780534552985.

APPENDIX A

Appendix A: Source Characteristics

- Frequency: 100 GHz.
- Beam shape: Gaussian.
- Beam diameter: 7 mm.
- Beam divergence: 18°.
- Antenna Gain: 20 dB.
- Typical VSWR: <1.2.
- Direction diagram:

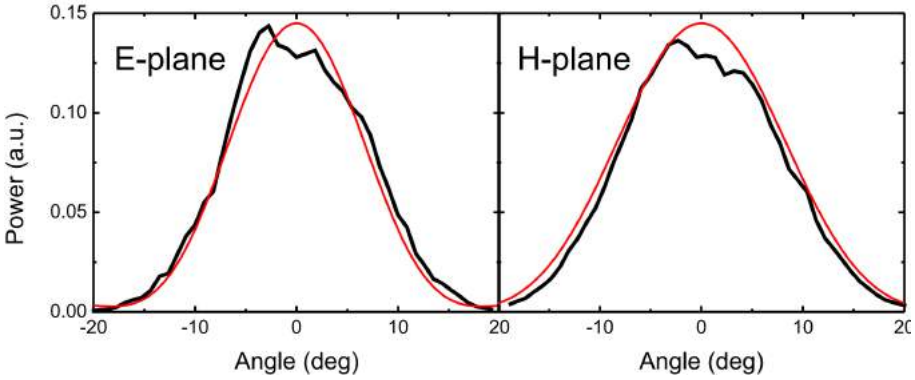

APPENDIX B

Appendix B: Normalised Source Scans

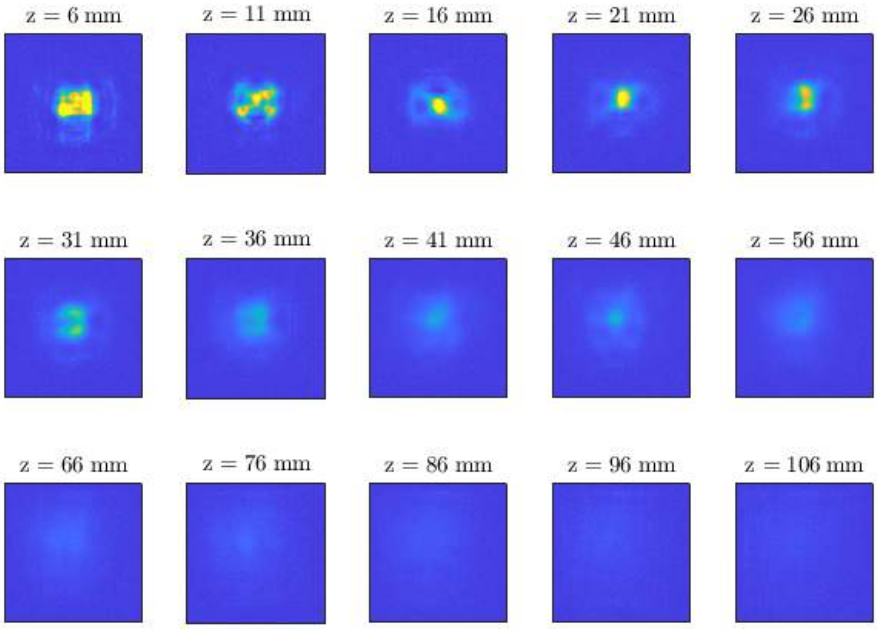

Appendix C

Appendix C: Fabry-Perot Code

Listing C.1: Fabry-Perot MATLAB^{TM} Code

```
set(groot,'defaultAxesTickLabelInterpreter','latex');
set(groot,'defaulttextinterpreter','latex');
set(groot,'defaultLegendInterpreter','latex'); % ^^^ Set latex as the text interpreter

n1 = 1; % Air
n2 = 1.6; % Material
n3 = 4.5; % Detector
n4 = 5; % Source

lambda = 3.2; % Wavelenght on air
width = 35.9;
thick = 7.8; % linspace(5,8,100);
def_thick = 2.0; %
def_pos = 4;
lower_pos = 10; % linspace(5,45,10000);

signal = zeros(50);
signal2 = zeros(50);
signal3 = zeros(50,1);

for d = 500:4500
    signal3(d-499) = multireflect(n1,n2,n3,n4,4, 35.6, d*0.01, lambda,1);
end

figure;
plot(signal3(1:500), "r");
ylim([0 1])
ylabel('$T = I_{out} / I_{in}$')
xticks([0 100 200 300 400 500])
```

```
xticklabels({'0','1','2','3','4','5'})
ax1 = gca;
axPos = ax1.Position;
ax1.Position = axPos + [0 0.3 0 -0.3];
ax2 = axes('position', (axPos .* [1 1 1 1e-3]) + [0 0.15 0 0]);
ax2.XLim = [0 5];
ax2.XTickLabel = {'5','4','3','2','1','0'};
ax1.XLabel.String = '$\Delta A$ (mm)';
ax2.XLabel.String = '$\Delta C$ (mm)';
set(gcf,'color','w');

for d = 1:50
    for p = 1:50

        signal(d-p+50,p) = multireflect(n1,n2,n3,n4,thick, width+(d*0.1-0.5), lower_pos+(p
            ↪ *0.1-0.2), lambda,0);

    end
end

for d = 1:50
    for p = 1:50

        signal2(d,p) = multireflect(n1,n2,n3,n4,thick, width+(d*0.1-0.5), lower_pos+(p
            ↪ *0.1-0.2), lambda,0);

    end
end

figure;
imagesc(signal);
daspect([1 1 1]);
set(gca,'YDir','normal');
set(gcf,'color','w');
h = colorbar;
ylabel(h, 'Relative Transmited Intensity')
xticks([0 10 20 30 40 50])
xticklabels({'0','1','2','3','4','5'})
yticks([0 20 40 60 80 100])
yticklabels({'0','2','4','6','8','10'})
xlabel(' $\Delta A$ (mm)')
ylabel(' $\Delta C$ (mm)')
%title('Calculated Eq.(4)')

figure;
imagesc(signal2);
daspect([1 1 1]);
set(gca,'YDir','normal');
set(gcf,'color','w');

```

```
figure;
surf(signal2);
set(gcf,'color','w');

function tot = multireflect(n1, n2, n3, n4, thick, width, lower_pos, lambda, at)
    A = lower_pos;
    B = thick;
    C = width - A - B;

    phi1 = 2*pi*A/lambda;
    phi2 = 2*pi*B*n2/lambda;
    phi3 = 2*pi*C/lambda;

    r1 = abs((n1-n4)/(n1+n4));
    r2 = abs((n1-n2)/(n1+n2));
    r3 = abs((n1-n2)/(n1+n2));
    r4 = abs((n2-n3)/(n2+n3));

    if at == 1
        at1 = 0.9;
        at2 = 0.8;
        at3 = 0.9;
    else
        at1 = 1;
        at2 = 1;
        at3 = 1;
    end

    at = sqrt(1-r1^2)*sqrt(1-r2^2)*sqrt(1-r3^2)*sqrt(1-r4^2)./ ...
        ( exp(1i*(-phi1-phi2-phi3)) ...
        + (at1*at1) * r1*r2 * exp(1i*(phi1-phi2-phi3)) ...
        + (at2*at2) * r2*r3 * exp(1i*(-phi1+phi2-phi3)) ...
        + (at1*at1*at2*at2) * r1*r3 * exp(1i*(phi1+phi2-phi3)) ...
        + (at3*at3) * r3*r4 * exp(1i*(-phi1-phi2+phi3)) ...
        + (at1^2)*(at2^4)*(at3^2) * r1*r2*r3*r4 * exp(1i*(phi1-phi2+phi3)) ...
        + (at3*at2*at3*at2) * r2*r4 * exp(1i*(-phi1+phi2+phi3)) ...
        + (at1^2)*(at2^2)*(at3^2) * r1*r4 * exp(1i*(phi1+phi2+phi3)));

    tot = at * conj(at);

end
}
```

APPENDIX D

Appendix D: Parameters of Simulated Materials

Source Antenna

Properties of the Material

	Name	Type	Value	Units
	Relative Permittivity	Simple	1	
	Relative Permeability	Simple	1	
	Bulk Conductivity	Simple	1e+030	siemens/m
	Dielectric Loss Tangent	Simple	0	
	Magnetic Loss Tangent	Simple	0	
	Magnetic Saturation	Simple	0	tesla
	Lande G Factor	Simple	2	
	Delta H	Simple	0	A_per_meter
	- Measured Frequency	Simple	9.4e+009	Hz
	Mass Density	Simple	0	kg/m^3

Detector and Copper Wire

Properties of the Material

	Name	Type	Value	Units
	Relative Permittivity	Simple	1	
	Relative Permeability	Simple	1.000021	
	Bulk Conductivity	Simple	38000000	siemens/m
	Dielectric Loss Tangent	Simple	0	
	Magnetic Loss Tangent	Simple	0	
	Magnetic Saturation	Simple	0	tesla
	Lande G Factor	Simple	2	
	Delta H	Simple	0	A_per_meter
	- Measured Frequency	Simple	9.4e+009	Hz
	Mass Density	Simple	2689	kg/m^3

Air

Properties of the Material

	Name	Type	Value	Units
	Relative Permittivity	Simple	1	
	Relative Permeability	Simple	1	
	Bulk Conductivity	Simple	0	siemens/m
	Dielectric Loss Tangent	Simple	0	
	Magnetic Loss Tangent	Simple	0	
	Magnetic Saturation	Simple	0	tesla
	Lande G Factor	Simple	2	
	Delta H	Simple	0	A_per_meter
	- Measured Frequency	Simple	9.4e+009	Hz
	Mass Density	Simple	0	kg/m^3

PLA

Properties of the Material

	Name	Type	Value	Units
	Relative Permittivity	Simple	4.3	
	Relative Permeability	Simple	1	
	Bulk Conductivity	Simple	0	siemens/m
	Dielectric Loss Tangent	Simple	0.004	
	Magnetic Loss Tangent	Simple	0	
	Magnetic Saturation	Simple	0	tesla
	Lande G Factor	Simple	2	
	Delta H	Simple	0	A_per_meter
	- Measured Frequency	Simple	9.4e+009	Hz
	Mass Density	Simple	0	kg/m^3

Water

Properties of the Material

	Name	Type	Value	Units
	Relative Permittivity	Simple	81	
	Relative Permeability	Simple	0.999991	
	Bulk Conductivity	Simple	0.01	siemens/m
	Dielectric Loss Tangent	Simple	0.9	
	Magnetic Loss Tangent	Simple	0	
	Magnetic Saturation	Simple	0	tesla
	Lande G Factor	Simple	2	
	Delta H	Simple	0	A_per_meter
	- Measured Frequency	Simple	9.4e+009	Hz
	Mass Density	Simple	997.4	kg/m^3